

Numerical simulation of artificial microswimmers driven by Marangoni flow

L. Stricker¹

¹*Max Planck Institute for Dynamics and Self-Organization (MPI DS), 37077 Göttingen, Germany*

In the present paper the behavior of a single artificial microswimmer is addressed, namely an active droplet moving by Marangoni flow. We provide a numerical treatment for the main factors playing a role in real systems, such as advection, diffusion and the presence of chemical species with different behaviors. The flow field inside and outside the droplet is modeled to account for the two-way coupling between the surrounding fluid and the motion of the swimmer. Mass diffusion is also taken into account. In particular, we consider two concentration fields: the surfactant concentration in the bulk, i.e. in the liquid surrounding the droplet, and the surfactant concentration on the surface. The latter is related to the local surface tension, through an equation of state (Langmuir equation). We examine different interaction mechanisms between the bulk and the surface concentration fields, namely the case of insoluble surfactants attached to the surface (no exchange between the bulk and the surface) and soluble surfactants with adsorption/desorption at the surface. We also consider the case where the bulk concentration field is in equilibrium with the content of the droplet. The numerical results are validated through comparison with analytical calculations. We show that our model can reproduce the typical pusher/puller behavior presented by squirmers. It is also able to capture the self-propulsion mechanism of droplets driven by Belousov-Zhabotinsky (BZ) reactions, as well as a typical chemotactic behavior.

I. INTRODUCTION

Unicellular swimmers, e.g., *E. coli* bacteria, spermatozoa, or paramecia are typically of a few to several ten micrometers in size and their swimming velocities are of the order of one body length per second. Due to their small size and swimming velocities, the Reynolds number of the flow involved in their swimming is much smaller than unity. As a consequence, viscous damping by far dominates over inertia, and the physics ruling their swimming is very different from that applying to swimming in the macro-world [1–3]. While inertia is the dominant propulsion mechanism for swimming in the macro-world, microorganisms make use of the viscous drag of the surrounding fluid for their propulsion. Initiated by the non-trivial nature of viscosity-based swimming and its important applications in biology, the study of the fundamental physics of swimming at low Reynolds numbers has become an active field of research during the past 40 years [1, 4–7].

Several kinds of artificial microswimmers have been produced, based on different mechanisms [8, 9], with a potential for technological applications such as target drug delivery, removal of pollutants, waste treatment. Examples of artificial microswimmers consist in active liquid droplets immersed in a second immiscible liquid and propelled by Marangoni flow. The underlying idea is to create a non-uniform surface tension distribution on the droplet surface, through a non-uniform distribution of surfactants, i.e. molecules of a third kind dissolved inside the solution and migrating to the surface [10]. To satisfy the local balance of forces at the interface, a Marangoni stress originates, tangent to the surface, from the area with a lower surface tension to the one with a higher surface tension. From this, a convective fluid motion is set inside and outside the droplet and, therefore the droplet starts moving.

Such surface tension gradients can rise (a) from chemical reactions changing either the structure of the surfactant molecules [11–14] or the surfactant coverage [15, 16] as well as (b) by dissolution or phase separation phenomena under non-equilibrium conditions [17, 18]. Intriguing systems have been produced, based on such principles, such as self-propelled droplets driven by Belousov-Zhabotinsky (BZ) reactions [19, 20], behaving like non-equilibrium chemical oscillators. Some experiments showed that nematic liquid crystal droplets, immersed in a solution of water/ionic surfactant, can develop spontaneous motion [21]. Also in this case, the propulsion mechanism appears to be a Marangoni flow, originating from a combined effect of the surfactants and the liquid crystals (i.e. non isotropic molecules) perpendicularly anchoring to the surface. The details of this mechanism are still unknown.

Active droplets moving by Marangoni flow can be considered "squirmers", i.e. swimmers where a tangential velocity of the surface drives propulsion. Theoretical works on this class of swimmers have investigated the velocity field generated by individual squirmers [22, 23], their hydrodynamic interactions [24, 25], and the resulting collective behavior [26]. The majority of this works assumes a prescribed fluid flow at the surface, instead of deriving it. However, for self-propelled droplets driven by gradients of mass concentration or temperature [27, 28] or by Belousov-Zhabotinsky (BZ) reactions [19], as well as for emulsion droplets [29, 30] of the kind described in [21], analytical solutions of the flow profiles are available for simplified cases, and the stability analysis of their motion has been addressed [31–35].

The description of more realistic scenarios requires to account for a large number of factors, such as the two-way coupling between the flow and the active droplet, several mutually interacting chemical species, mass exchanges between the droplet's interface and the surrounding liquid (bulk), chemical reactions. In such cases, the numerical approach can be a powerful instrument to investigate the problem at hand.

Several numerical techniques have been developed during the last decades, to track the motion of interfaces: (i) "interface tracking methods", where the displacement of the interface is tracked in a direct-fashion, e.g. through a set of Lagrangian marker points located on the surface itself (front-tracking [36]) (ii) "interface capturing methods", where the motion of the interface is described in an implicit-fashion, by following the evolution of an additional function; examples are: immersed boundary [37], finite elements (FEM) [38], volume of fluid (VOF) [39], marker-and-cell [40], level set [41, 42] and hybrid methods such as VOF/level set [43]. Combined approaches between (i) and (ii) have also been adopted in order to simultaneously address the interface motion, the flow field around the interface and the surfactant diffusion on the surface. For instance, Lagrangian points marking the interface have been used in combination with a finite difference method for the evolution of the surfactant distribution on the interface and a boundary integral method for the Stokes equations in the fluid [44]. In the present paper, we use a level set approach [45–48] with a continuous surface force formulation [49], in combination with a flow solver based on a projection method [50] to track the motion of the fluid both inside and around the droplet. A vast literature is available for level set methods, including some books [46, 48]. For a review, we refer the reader to Ref. [47]. Level set methods have proven particularly efficient when singularities and disconnected bodies are present [51–53]. They allow for the treatment of deformable droplets as well as for a straightforward extension to the case of multiple swimmers. Several authors have numerically studied biphasic systems with surfactants using different methods: arbitrary LagrangianEulerian [43], VOF [39], finite difference/front-tracking [54–57], the diffuse-interface or phase-field method [58]. However, to our knowledge, only few have made use of a level-set formulation, either for the case of insoluble [41, 59, 60] or soluble [61] surfactants.

The aim of the present work is to provide a numerical model that could be adapted to the study of real artificial microswimmers moving by Marangoni flow, such as BZ-reaction driven droplets [19, 20, 35] and emulsion droplets of the kind described in [21]. The description of these systems requires to account for the two-way coupling between the droplet's motion and the fluid flow, as well as multiple mutually interacting concentration fields (e.g.: empty micelles, filled micelles, liquid crystals, molecular

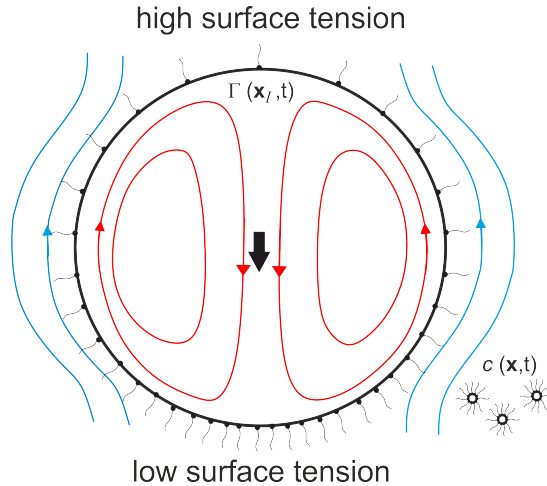


FIG. 1. Schematic sketch of a droplet moving by Marangoni flow. A surfactant field is present both on the interface, namely Γ , and in the liquid surrounding the droplet (bulk), c , in micellar form. The grey lines (red and light-blue online) represent the flow field inside (red online) and outside the droplet (light-blue online). The thick black arrow indicates the direction of the droplet's motion.

surfactant [21, 29]). We wish to provide here a numerical treatment for the main phenomena playing a role in such systems: the flow field, the surfactant advection and diffusion, both in the liquid bulk and on the surface of the droplet, as well as the interaction between the bulk and the surface (adsorption/desorption). The case where a concentration field dissolved inside the bulk is in equilibrium conditions with a droplet of the same substance (e.g. liquid crystals in the emulsion droplets of [21]) is also addressed.

In Fig. 1 we display a simplified sketch of a possible scenario addressed by our code, where an active droplet moves by Marangoni flow. A surfactant concentration field is present, both on the surface of the droplet Γ and in the bulk c . The non-uniform surface concentration induces a non-uniform surface tension field on the surface. In particular, a higher concentration of surfactant corresponds to a lower surface tension, since the surfactants produce a local 'weakness' at the interface. Through a local force balance, one can see that a tangential flow originates at the interface - see grey lines (red and light-blue online) - both inside (red online) and outside the droplet (light blue online). By momentum conservation, the droplet moves in the direction indicated by the thick black arrow. The presence of surfactant concentration fields only outside the droplet and on the surface yields the one-sided nature of the problem. Based on embedded finite difference schemes, our work presents a novel treatment of such a situation.

II. MODEL

We consider a 3D geometry, under the assumption of axial symmetry. The computational domain is fixed and divided in $N_r \times N_z$ cells, of sides $\Delta r = \Delta z = h$, where r is the radial coordinate and z is the axial coordinate. A level set description is adopted to track the position of the interface separating the liquid inside the droplet (oil or liquid crystals) and the surrounding medium (water). The level set function Φ is a smooth function defined at the center of each computational cell. We use a "narrow band" approach [46], therefore Φ is defined only inside a shell S_Φ , with width $2\Delta_\Phi$ where $\Delta_\Phi = 15h$, located around the interface. Φ assumes positive values outside the droplet and negative values inside. The droplet's interface is implicitly defined as the set of points where $\Phi = 0$. In order to simplify the numerical treatment, the level set function is chosen with the particular property of being a signed distance function. Its absolute value in each point \mathbf{x} of the domain is equal to the shortest distance between \mathbf{x} and the interface I

$$\Phi(\mathbf{x}) = S(\Phi(\mathbf{x}))\min(|\mathbf{x} - \mathbf{x}_I|), \quad \forall \mathbf{x}_I \in I \quad (1)$$

where \mathbf{x}_I is a point on the interface and $S(\Phi)$ is the sign of the level set function

$$S(\Phi) = \begin{cases} 1, & \text{if } \mathbf{x} \text{ outside droplet} \\ 0, & \text{if } \mathbf{x} \text{ on surface} \\ -1, & \text{if } \mathbf{x} \text{ inside droplet} \end{cases} \quad (2)$$

With this specific choice for the level set function, the unit normal vector \mathbf{n} , perpendicular to the surface at each point, is

$$\mathbf{n} = \frac{\nabla\Phi}{|\nabla\Phi|}, \quad (3)$$

and the local (3D) curvature κ can be derived as

$$\kappa = -\nabla \cdot \mathbf{n} \quad (4)$$

A. Dynamics

We solve the Navier-Stokes equation inside and outside the droplet, to derive the velocity field $\mathbf{u}(t, \mathbf{x})$ and the pressure field $p(t, \mathbf{x})$, as a function of time, t

$$\rho \left[\frac{\partial \mathbf{u}}{\partial t} + \mathbf{u} \cdot \nabla \mathbf{u} \right] = -\nabla p + \nabla \cdot [\mu(\nabla \mathbf{u} + \nabla \mathbf{u}^T)] + \delta(\Phi)(-\kappa \sigma \mathbf{n} + \nabla_s \sigma), \quad (5)$$

We close the set of equations by the incompressibility condition

$$\nabla \cdot \mathbf{u} = 0 \quad (6)$$

In the former equation, σ is the surface tension, κ is the local curvature, $\nabla_s = (I - \mathbf{n} \otimes \mathbf{n})\nabla$ is the surface gradient and $\delta(\Phi)$ is the surface delta function. The viscosity μ and the density ρ of the liquid are assumed to be constant both inside and outside the droplet. In the numerical treatment of Eq. (5), we use a smeared delta function δ_ϵ instead of δ [61]

$$\delta_\epsilon(x) = \begin{cases} \frac{1}{2\epsilon} (1 + \cos \frac{\pi x}{\epsilon}), & \text{if } |x| \leq \epsilon \\ 0, & \text{else} \end{cases} \quad (7)$$

In our simulations, we take $\epsilon = 1.5h$, with h the length of the side of a computational cell.

The last term in Eq. (5) can be seen as a local force acting only on the interface. It is due to both the surface tension and its gradient along the interface, the Marangoni stress. This formulation, the so-called *continuum surface force formulation* [49], is convenient in order to enforce the boundary condition for the stresses at the interface, without explicitly using a jump condition [58, 60]. We note that, from the physical point of view, the surface tension is defined only at points \mathbf{x}_I belonging to the interface I . However, in order to facilitate the numerical treatment, we adopt a fictitious surface tension field $\sigma(\mathbf{x})$, defined at the centre of the computational cells, in a neighborhood of the interface. The value of σ at a generic point \mathbf{x} of the computational domain corresponds to the physical value of the surface tension at the closest point \mathbf{x}_I on the interface and it is derived from an extended surface concentration field of the surfactants as described below.

The surface tension is related to the local surface concentration of the surfactants Γ through the Langmuir equation of state [62]

$$\sigma(\Gamma) = \sigma_0 + \mathcal{R}T\Gamma_\infty \log(1 - \Gamma/\Gamma_\infty) \quad (8)$$

where σ_0 is the surface tension for a clean interface ($\Gamma = 0$), Γ_∞ is the saturation concentration, i.e. the maximum surfactant packing on the surface, R is the ideal gas constant and T is the temperature, expressed in Kelvin. Eq. (8) provides a good description for low values of the surface concentration ($\Gamma \ll \Gamma_\infty$) but it has reduced accuracy otherwise. To prevent unphysical negative surface tension, resulting into an instability of the interface, we modify Eq. (8) [55] as

$$\sigma(\Gamma) = \sigma_0 \left[\max \left(\epsilon_\sigma, 1 + \beta_s \log(1 - \Gamma/\Gamma_\infty) \right) \right] \quad (9)$$

where $\epsilon_\sigma = 0.05$ in our simulations and $\beta_s = \mathcal{R}T\Gamma_\infty/\sigma_0$ is the elasticity number, quantifying the sensitivity of the surface tension to surface concentration variations. In our treatment, the fictitious field $\sigma(\mathbf{x})$ is computed cell by cell, from the values of another fictitious extended field $\Gamma(\mathbf{x})$, representing the local surface concentration of the surfactants at the closest point of the interface \mathbf{x}_I . We refer the reader to Sec. II C 1 for the derivation of such a field, from the real surface concentration at the interface, $\Gamma(\mathbf{x}_I)$.

The equations of momentum (5) and mass (6) conservation are solved with a projection method [50]. We use a standard staggered grid for the pressure and the velocity fields, with the pressure defined at the center of the computational cells and the velocity components on the walls of the computational cells. In particular for each computational cell, the radial component of the velocity, u , is defined at the center of vertical walls, while the axial component of the velocity, v is defined at the center of

horizontal walls. At the time instant n , the momentum equation (5) is numerically integrated by means of two separate steps, introducing an intermediate velocity field \mathbf{u}^* . The first intermediate step consists of a *predictor step*, where both the advective and the diffusive term are treated explicitly. \mathbf{u}^* is found with a first order Euler method:

$$\frac{\mathbf{u}^* - \mathbf{u}^n}{\Delta t} = -(\mathbf{u} \cdot \nabla \mathbf{u})^n + \frac{1}{\rho}(\nabla \cdot \mathbf{D} + \mathbf{F})^n, \quad (10)$$

where $\mathbf{D} = \mu 6(\nabla \mathbf{u} + \nabla \mathbf{u}^T)$ and $\mathbf{F} = \delta(\Phi)(-\kappa \sigma \mathbf{n} + \nabla_s \sigma)$. In order to prevent instabilities arising from the explicit treatment, the time step Δt is chosen according to the CFL condition, so that at each time step the displacement of the interface will not be larger than one grid cell [63]

$$\Delta t = \epsilon_\tau \min(\tau_{adv}, \tau_{visc}, \tau_{surf}, \tau_{grav}) \quad (11)$$

where $\epsilon_\tau = 0.25$ and $\tau_{adv}, \tau_{visc}, \tau_{surf}, \tau_{grav}$ are the time scales to displace the fluid of one grid cell by advection, viscosity and capillarity, respectively

$$\tau_{adv} = \left(\frac{|u_r|_{max}}{\Delta r} + \frac{|u_z|_{max}}{\Delta z} \right)^{-1}, \tau_{visc} = \frac{\rho}{2\mu} \left(\frac{1}{\Delta r^2} + \frac{1}{\Delta z^2} \right)^{-1}, \tau_{surf} = \left(\frac{\sigma}{\rho \Delta r^3} \right)^{-1/2}. \quad (12)$$

As \mathbf{u}^* is not divergence-free, a *projection step* is required, to find the real field \mathbf{u}^{n+1} at time $n + 1$

$$\frac{\mathbf{u}^{n+1} - \mathbf{u}^*}{\Delta t} = -\frac{\nabla p^{n+1}}{\rho}. \quad (13)$$

In order to calculate the pressure field p , we apply the divergence operator to both sides of Eq. (13), imposing the desired property that the final velocity field is divergence-free, $\nabla \cdot \mathbf{u}^{n+1} = 0$. Thus we obtain the Poisson equation

$$\frac{1}{\rho} \nabla^2 p^{n+1} = \frac{\nabla \cdot \mathbf{u}^*}{\Delta t}. \quad (14)$$

This equation has to be solved subject to the boundary conditions: $\frac{\partial p}{\partial r}|_{r=0} = 0$ at the z-axis, for symmetry reasons; at the other limits of the computational domain, we consider a Dirichlet boundary condition $p = p_\infty$ for open flows and a Neumann boundary condition $\mathbf{n} \cdot \nabla p = 0$ for rigid walls. In the integration of Eq. (10), the spatial derivatives of \mathbf{u}^n in the advective term are calculated by means of a third-order ENO scheme [45].

B. Kinematics

The value of the level set function associated to a certain material point must not change when such a point moves along the trajectory followed by the interface. Therefore, the level set function is advected by means of the equation [47, 48]

$$\frac{\partial \Phi}{\partial t} + \mathbf{u}_{ext} \cdot \nabla \Phi = 0, \quad (15)$$

in which, \mathbf{u}_{ext} is an extended velocity field, derived from the real fluid velocity field \mathbf{u} at the interface. In the proximity of the interface \mathbf{u}_{ext} corresponds to the real velocity field. In the far field, a rigid translation of the interface velocity in the normal direction to the interface itself has been adopted. In principle, one could use the real velocity field of the fluid, \mathbf{u} , for the advection of the level set function [47]. However, this method would cause the level set function to lose its property of being a signed distance function, which should then be reinforced at every time iteration by mean of additional numerical manipulations [64–67], which are however known to cause mass losses [65, 68]. To avoid such a problem, we construct an extended velocity field with the above-mentioned properties and we use it to perform a rigid-like advection of the level set [69]. Several procedures have been proposed so far to extend a quantity from an interface, mostly involving the solution of a PDE on the whole computational domain [69–72]. In the present paper, we use a different approach. We consider a point P located in \mathbf{x}_P , at the center of a computational cell, where we want to derive the extended velocity field $\mathbf{u}_{ext,P}$. We calculate the location \mathbf{x}_I of the closest point I of the interface, using the signed distance property of the level set function

$$\mathbf{x}_I = \mathbf{x}_P - \Phi_P \mathbf{n}_P. \quad (16)$$

We derive the velocity \mathbf{u}_I at point I of the interface with the method described below and we impose $\mathbf{u}_{ext,P} = \mathbf{u}_I$. In order to derive \mathbf{u}_I , we use a linear interpolation technique based on a Lagrangian multiplier formulation [63]. In particular, we assume that the approximated velocity $\tilde{\mathbf{u}}$ at a generic location \mathbf{x} in the neighborhood of point I could be written as

$$\tilde{\mathbf{u}}(\mathbf{x}) \simeq \mathbf{u}_I + \nabla \mathbf{u}_I \cdot (\mathbf{x} - \mathbf{x}_I), \quad (17)$$

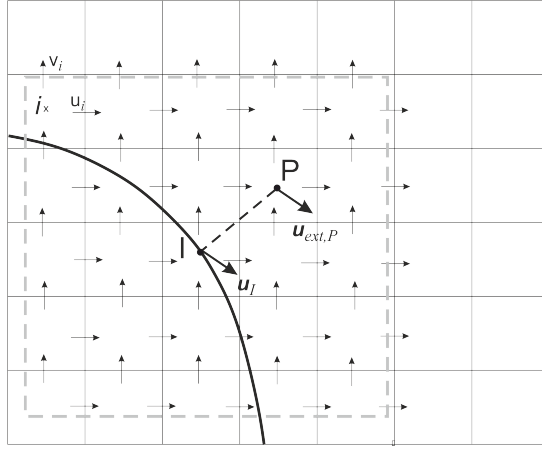


FIG. 2. Sketch of the points used to derive the extrapolated velocity at point P , $\mathbf{u}_{ext,P} = \mathbf{u}_I$, to be used for the advection of the level set function. The interface velocity \mathbf{u}_I is computed based on the calculated velocities in the cells enclosed by the dashed grey line, whose radial and axial components, u and v , are depicted by the horizontal and vertical arrows respectively.

where \mathbf{u}_I is the velocity at point I , still unknown. We consider a portion of the computational domain, namely a square of $N_s \times N_s$ cells around \mathbf{x}_I (see the area delimited by the grey dashed line in Fig. 2). We then write the Lagrangian function \mathcal{L} as

$$\mathcal{L} = \mathcal{L}_0 + \lambda \mathcal{Q}, \quad (18)$$

where λ is another unknown parameter, $\mathcal{Q} = \nabla \cdot \mathbf{u}_I$ represents the constraint of the velocity field being divergence-free at the interface and

$$\mathcal{L}_0 = \sum_i^{N_s \times N_s} (\tilde{\mathbf{u}}_i - \mathbf{u}_i)^2, \quad (19)$$

with i denoting the different points and $\tilde{\mathbf{u}}_i$ expressed by substituting the values \mathbf{x}_i inside Eq. (17). We minimize the Lagrangian function \mathcal{L} by solving the system

$$\nabla \mathcal{L} = 0, \quad (20)$$

where the unknowns are \mathbf{u}_I , $(\frac{\partial \mathbf{u}}{\partial r})_I$, $(\frac{\partial \mathbf{u}}{\partial z})_I$ and λ . Hence we find the desired interpolated value of the velocity at the interface \mathbf{u}_I and we rigidly transport it in \mathbf{x}_P , finding $\mathbf{u}_{ext,P}$ (see Fig. 2). The present method is more precise respect to a standard bilinear interpolation, as it allows for the possibility to add the divergence-free constraint of the values of the interpolated velocity at the interface.

Once we have derived the extended velocity field, the advection of the level set function is performed by integrating in time Eq. (15) with a second-order Adam-Bashforth scheme

$$\frac{\Phi^{n+1} - \Phi^n}{\Delta t} = -\frac{3}{2}(\mathbf{u} \cdot \nabla \Phi)^n + \frac{1}{2}(\mathbf{u} \cdot \nabla \Phi)^{n-1}, \quad (21)$$

in which the superscript indicates the time instant. The spatial derivatives of Φ are computed with a fifth-order WENO scheme [73].

After advecting the level set, a correction of Φ may still become necessary in order to enforce the signed-distance property. This manipulation, called *reinitialization*, must not displace the interface and it can be performed in different ways [64–67]. However, due to undesired interface displacements, the reinitialization step is known to cause mass loss. Several solutions have been proposed for this problem [65, 68, 74–77]. Here, the use of an extended velocity field of the kind described above for the advection of the level set, allows us to consistently reduce the number of required reinitialization steps [64, 67, 72, 78]. Since $|\nabla \Phi| = 1$ for a signed distance function, we perform a reinitialization when $|\nabla \Phi|$ differs from 1 more than $\epsilon = 10^{-4}$. As a direct calculation of the zero level set [64] is computationally expensive, in the present work we adopt a modified version of the method of Ref. [65], solving the equation

$$\begin{aligned} \frac{\partial \Phi}{\partial \tau} + S(\Phi^0)(1 - |\nabla \Phi|) &= 0 \\ \Phi(\mathbf{x}, 0) &= \Phi^0(\mathbf{x}, 0), \end{aligned} \quad (22)$$

until steady state is reached. Here τ is an artificial time and Φ^0 is the level set function calculated with Eq. (15).

Eq. (22) is integrated in the pseudo-time τ with the third-order Runge-Kutta scheme described in [79], consisting of a linear combination of Euler integration steps:

$$\begin{aligned}\Phi^{(1)} &= \Phi^t - \Delta\tau L\Phi^t, \\ \Phi^{(2)} &= \frac{3}{4}\Phi^t + \frac{1}{4}\Phi^{(1)} - \frac{1}{4}\Delta\tau L\Phi^{(1)}, \\ \Phi^{t+1} &= \frac{1}{3}\Phi^t + \frac{2}{3}\Phi^{(2)} - \frac{2}{3}\Delta\tau L\Phi^{(2)},\end{aligned}\tag{23}$$

with the superscript t denoting the pseudo-time step, $L\Phi^{(k)} = S(\Phi^0)(|\nabla\Phi^{(k)}| - 1)$. In order to further reduce the mass loss associated to the reinitialization, particular care has been taken in the calculation of $\nabla\Phi$ at points adjacent to the interface, when solving Eq. (22). Here the spatial derivatives of Φ are computed using the "subcell fix" method described in Refs. [63, 74]. With this method, the spatial derivatives of Φ at point \mathbf{x} are calculated with a fifth-order WENO scheme, when \mathbf{x} is far from the interface, and with a third-order modified ENO scheme when \mathbf{x} is close to the interface. The modified ENO schemes uses an asymmetric stencil, which includes the closest point of the interface along the direction of the partial derivative that we are calculating. Such an interface point corresponds to a level set value known and null; its position is retrieved by cubic interpolation along the considered direction. This method is conceptually equivalent to solving Eq. (22) on two separate domains, inside and outside the droplet, with Dirichlet boundary condition $\Phi = 0$ at the interface. The above-mentioned procedure is essential to guarantee the upwind nature of the scheme, i.e. to avoid transfer of information across the interface. It makes use of the fact that the reinitialization equation is a hyperbolic equation, such that its characteristics always propagate from the interface to the liquid [63].

C. Mass transport processes

1. Surface concentration field Γ

The evolution of the surfactant concentration on the surface is described by an advection-diffusion equation. The space-wise implicit nature of the level set formulation, does not allow for an explicit treatment of a surface concentration field located at the interface. Therefore, in line with the spirit of the level-set method, we consider a fictitious field Γ , defined at the center of the cells of the computational domain in a neighborhood of the interface (within a shell $S_\Gamma = 2\Delta$ with $\Delta = 10h$). This extended field is built in such a way that its interpolated values correspond to the surface concentration at the interface. In particular, at each point P of the computational domain, the value of Γ represents the value of the surface concentration at the closest point of the interface, I . Following a derivation outlined in [60, 80], we rewrite the local mass conservation equation as

$$\frac{\partial\Gamma}{\partial t} + \mathbf{u}_{ext} \cdot \nabla\Gamma + \Gamma\nabla \cdot \mathbf{u}_{ext} - \mathbf{n} \cdot (\nabla\mathbf{u}_{ext}\mathbf{n})\Gamma = D_s\nabla_s^2\Gamma + j\tag{24}$$

where D_s is the surface diffusivity and $\nabla_s^2\Gamma = \nabla^2\Gamma - \mathbf{n} \cdot (\nabla\nabla\Gamma)\mathbf{n} - \kappa\mathbf{n} \cdot \nabla\Gamma$ is the surface Laplacian. The term $-\mathbf{n} \cdot (\nabla\mathbf{u}_{ext})\Gamma$ accounts for the change in the surface concentration due to the change in the local curvature. The advection velocity of the level-set function \mathbf{u}_{ext} (see Eq. (15)) describing the velocity at the interface, is used for the advection of the surface concentration field; the term j describes the net exchange of surfactant with the bulk field [58]

$$j = r_a(\Gamma_\infty - \Gamma)c_I - r_d\Gamma\tag{25}$$

Here r_a and r_d are the adsorption and desorption rate, respectively, Γ_∞ is the surface saturation concentration and c_I is the bulk concentration at the interface. The concentration field in the bulk c is defined at the center of the computational cells in the liquid outside the droplet. Unlike Γ , c is not a fictitious field and its values indicates a local concentration at the point where they are defined. Hence, for the calculation of j by Eq. (25) at a generic point $P \in S_\Gamma$ of the domain, $\Gamma(\mathbf{x}_P)$ gives the desired value of the surface concentration at the closest point of the interface I by construction, but the corresponding bulk concentration c_I still needs to be calculated. To this aim, we adopt a procedure based on a Lagrangian multiplier method, similar to the one we used to derive the extended velocity field \mathbf{u}_{ext} (see Eqs. (15)-20). We first derive the position of the closest interface point I , by Eq. (16). We assume that the approximated bulk concentration \tilde{c} at a generic location \mathbf{x} in the neighborhood of point I could be written as

$$\tilde{c}(\mathbf{x}) \simeq c_I + \nabla c_I \cdot (\mathbf{x} - \mathbf{x}_I) + (\mathbf{x} - \mathbf{x}_I)^T \cdot \mathbf{D}_2(c) \cdot (\mathbf{x} - \mathbf{x}_I),\tag{26}$$

where \mathbf{D}_2 denotes the Hessian matrix. The Lagrangian function is defined as

$$\mathcal{L} = \mathcal{L}_0 = \sum_i^{N_p} (\tilde{c}_i - c_i)^2,\tag{27}$$

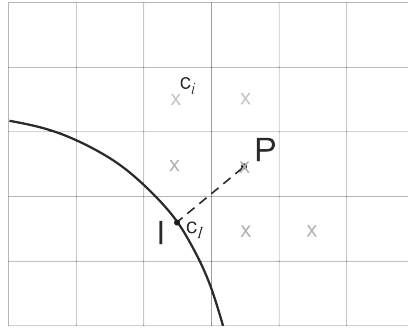


FIG. 3. Sketch of the points used to infer the interpolated bulk concentration at point I , c_I , required for the calculation of the source term j at point P (see Eq. (25)). The grey crosses represent the values of the bulk concentrations used to derive c_I .

with N_p the number of valid points, i.e. points where $\Phi > 0$ and the field c has a physical meaning. The N_p points are chosen based on a minimum distance criterium from the point I itself, i.e. we take the N_p closest points to I (see Fig. 3). The fitting function \tilde{c} is found again by solving the system $\nabla \mathcal{L} = 0$. Hence we know c_I . We remark that this procedure was adopted in order deal with both the one-sided nature of the problem and the stiff gradients of the bulk concentration field, that may originate close to the interface. We verified that, in a case like this, where one wishes to find a one-sided interpolation respect to an interface, this method gives better results respect to a standard bicubic interpolation based on a 16 points stencil as it requires a lower number of points N_p . In our simulations we took $N_p = 6$ and we checked that this was enough to provide good results.

Eq. (24) is integrated in a semi-implicit fashion, by solving the linear system

$$\frac{\Gamma^{n+1} - \Gamma^n}{\Delta t} = \frac{3}{2}R^n - \frac{1}{2}R^{n-1} + D_s \left(\frac{1}{2}\nabla_s^2 \Gamma^{n+1} + \frac{1}{2}\nabla_s^2 \Gamma^n \right) \quad (28)$$

where $R^n = [-\mathbf{u} \cdot \nabla \Gamma + \mathbf{n} \cdot (\nabla \mathbf{u}) \Gamma + j]^n$. The superscripts n and $n - 1$ indicate the present and the previous time instants, respectively, where all the quantities are known, while $n + 1$ is referred to the next time step, therefore to unknown quantities. The spatial derivatives of Γ in the explicit advective term are computed with a fifth-order WENO scheme [73]. For the derivatives in the diffusive implicit term, we adopt a standard second order centered difference formulation. At the borders of the area S_Γ we impose a Neuman boundary condition $\mathbf{n} \cdot \nabla \Gamma = 0$. The linear system deriving from the discretization of Eq. (28) is solved by means of a conjugate gradient method. We chose to use a semi-implicit solver in time, because it does not give rise to additional constraints on Δt respect to those imposed by the CFL condition (see Eqs. (11)-12). Thus it allows for larger time steps respect to an explicit method.

Similar to the advection of the level set function, there are discretization errors in the advection of the extended surface tension field. We hence need to correct the advected extended field Γ to ensure that the concentration values at the interface are properly transported along the characteristics. To this aim we adopt a scheme in the same spirt of the one described in Eqs. (22)-23 for the reinitialization of the level set function, i.e. we solve the following equation until steady state is reached [81]

$$\begin{aligned} \frac{\partial \Gamma}{\partial \tau'} + S(\Phi^0)(\mathbf{n} \cdot \nabla \Gamma) &= 0 \\ \Gamma(\mathbf{x}, 0) &= \Gamma^0(\mathbf{x}), \end{aligned} \quad (29)$$

where τ' is an artificial time and Γ^0 is the surface concentration calculated with Eq. (24). To solve Eq. (29) we use a third-order Runge-Kutta scheme. The spatial derivatives are calculated by means of a third-order ENO scheme.

2. Bulk concentration field c

The evolution of the surfactant concentration field c in the bulk, i.e. outside the droplet, is described by means of the advection-diffusion equation

$$\frac{\partial c}{\partial t} + \mathbf{u} \cdot \nabla c = D \nabla^2 c \quad (30)$$

where D is the diffusivity constant of the surfactant in the bulk. In order to avoid the introduction of a further limitation on the time step arising from an explicit treatment of the diffusive terms, these are treated implicitly. A second-order Adams-Bashfort scheme is adopted for the time integration

$$\frac{c^{n+1} - c^n}{\Delta t} = -\frac{3}{2}(\mathbf{u} \cdot \nabla c)^n + \frac{1}{2}(\mathbf{u} \cdot \nabla c)^{n-1} + D\nabla^2 c^{n+1} \quad (31)$$

As the purpose of the present work is the development of a model that could be adapted to the study of complex microswimmers, where several chemical species are present dissolved in the bulk and behave differently [19–21], we implemented different scenarios, corresponding to different boundary conditions for c at the droplet's interface \mathcal{I} . In the case that we have described so far, where a surfactant is dissolved inside the bulk and adsorbed/desorbed at the droplet's interface, a Neumann boundary condition is required, prescribing the normal flux $D(\mathbf{n}\nabla c)_I$ at the droplet's interface. This scenario applies, for example, to the surfactant fields in the system described in Refs. [20, 21]. Such a system consists of a liquid crystal droplet, immersed in a aqueous solution where surfactants are dissolved, both in micellar and molecular form. A complete treatment of these mutually-interacting fields is beyond the purpose of the present work. However, as we wish here to address all the basic mechanisms at play, we also present a model for the liquid crystal concentration field diffusing from the droplet into the liquid. As a consequence of such a diffusion process, the droplet will also shrink. However, the experiments showed that this process is slow compared to the droplet's motion and not visible during the time-scales we are interested in (of the order of seconds and minutes) [21]. Therefore, the droplet's shrinking will be neglected in our treatment. The evolution of the liquid crystals dissolved inside the water can be described by an equation of the same type of Eq. (30) with a Dirichlet boundary condition $c_I = c_0$ at the droplet's interface where c_0 is a constant equilibrium value. This model describes the equilibrium between the pure liquid crystal phase (inside the droplet) and the dissolved one (outside the droplet). In this case there is of course no surface concentration field coupled to the bulk field.

- Neumann boundary condition at the interface

When the bulk concentration field c and the surface concentration field interact with each other (e.g. by means of adsorption/desorption phenomena [20, 21]), we formulate the boundary condition at the interface as [58]

$$D(\mathbf{n} \cdot \nabla c)|_I = j \quad (32)$$

The left-hand side represents the net flux of c exchanged at the interface. It takes positive values when surfactant leaves the bulk and deposits on the surface. The right-hand side, j , is the increase rate of surfactant on the surface, as derived in Eq. (25). Formally, this exchange of concentration can be incorporated into Eq. (24) by adding a δ -function source term at the interface

$$\frac{\partial c}{\partial t} + \mathbf{u} \cdot \nabla c = D\nabla^2 c - \delta(\Phi)j \quad (33)$$

and revising the boundary condition at the interface to take the form $\mathbf{n} \cdot \nabla c|_I = 0$. This new boundary condition is enforced by fictitiously extending the field c inside the droplet, and using it to calculate the time-explicit advection term in Eq. (31). To perform this extension, we use the same method described in Sec. II C 1 for the extension of the Γ field: we solve to steady state an equation of the kind of Eq. (29), this time only inside the droplet. We note that the standard smeared version of delta function 7 has support on both sides of the interface. Therefore, in order to guarantee mass conservation, we need to adopt a new smeared delta function δ_+ , with support only on the outside of the droplet [82]. We define

$$\delta_+(x) = \begin{cases} 2\delta_\epsilon, & \text{if } 0 < x \leq \epsilon \\ 0, & \text{else} \end{cases} \quad (34)$$

This procedure has been proved to be rigorous in the one-dimensional case [82], since the above-defined δ_+ is a delta sequence function with the same distribution as the delta function. Unfortunately this property is not exactly fulfilled for generic higher-dimensional cases, as the numerical integration over the support does not give the exact value of 1. However, this approach can still provide good results within the expected second-order error convergence, as we show in Sec. III D.

- Dirichlet boundary condition at the interface

The implementation of a Dirichlet boundary condition, is carried out by means of an extrapolated "ghost" bulk concentration field inside the droplet, to be used for the calculation of the explicit advective term $(\mathbf{u} \cdot \nabla c)^n$ in Eq. (31). The adopted procedure is inspired by the one used in [63] for the treatment of the temperature field. The underlying idea is to first calculate the normal gradient at instant n , $c_n^n = (\mathbf{n} \cdot \nabla c)^n$ outside the droplet, by accounting for the Dirichlet boundary condition, then extrapolate it inside the droplet and finally use this extrapolated normal gradient field $c_{n,ext}^n$ to derive an extrapolated bulk concentration field c_{ext}^n . In detail, the procedure works as follows. We compute the physical normal gradient outside the droplet, by means of a centered differences second-order discretization. At points adjacent to the interface, we use a "cutcell method", i.e. we consider

a non-symmetric stencil including the interface. For example, for a generic point P just at the right of an interface point I , the discrete radial derivative at time instant n will be $\frac{\partial c}{\partial r}|_P^n = \frac{c_P - c_I}{\theta^n \Delta r}$, where $\theta^n = (r_P - r_I^n)/\Delta r$. The bulk concentration at the interface is given by the Dirichlet boundary condition $c_I = c_0$. After computing the normal gradient outside the droplet, we extend it inside the droplet, by solving to steady state the equation

$$\begin{aligned} \frac{\partial c_{n,ext}}{\partial \tilde{\tau}} - H(-\Phi^n)(\mathbf{n} \cdot \nabla c_{n,ext}) &= 0 \\ c_{n,ext}(\mathbf{x}, 0) &= c_n^n(\mathbf{x}), \end{aligned} \quad (35)$$

with $\tilde{\tau}$ an artificial time variable and H the Heaviside function. The integration of Eq. (35) in the pseudo-time is performed by means of a second-order Runge-Kutta scheme. The spatial derivatives of the normal gradient are computed with a second-order ENO scheme. From the extrapolated normal gradient $c_{n,ext}$, we derive the values of the extrapolated bulk concentration field inside the droplet by linear extrapolation, as $c_{ext} = c_I + \phi(\mathbf{n} \cdot c_{n,ext})$.

For the treatment of the time-implicit diffusive terms $D\nabla^2 c^{n+1}$, we also adopt a linear extrapolation of c^{n+1} inside the droplet, enforcing the boundary condition $c_I = c_0$, when writing the five-diagonal matrix for the Poisson solver. For example, for a grid point P , characterized by indexes i, j and laying at the right of the interface point I , the discretization of the Laplacian operator reads

$$\nabla^2 c_{i,j} \simeq \frac{1}{r_{ij}} \left(r_{i+1/2} \frac{c_{i+1,j} - c_{i,j}}{\Delta r} - r_{i-1/2} \frac{c_{i,j} - c_{i-1,j}^{ext}}{\Delta r} \right) + \frac{c_{i,j+1} - c_{i,j}}{\Delta z} - \frac{c_{i,j} - c_{i,j-1}}{\Delta z} \quad (36)$$

with $c_{i-1,j}^{ext} = c_{i,j} - \frac{c_{i,j} - c_I}{\theta \Delta r}$. Note that, in Eq. (36), we dropped the superscript $n+1$ everywhere for clarity, but the position of point I used in this discretization, r_I therefore θ , are those referred to the new time instant $n+1$, at this point already known from the solution of Eq. (15).

D. Chemical reactions

Despite providing some initial motion, in an isolated system, absorption-desorption alone cannot generate a proper self-sustained propulsion, since they basically only shift material from one place to another. Unless externally sustained (like in the case of chemotaxis, that will be discussed in Sec. IV D) the concentration gradients are eventually levelled up by diffusion and the droplet stops. In order to have an actual self-propulsion mechanism, one needs to consider some additional mechanism, where the energy is actively used. One possible way is through chemical reactions depleting the surfactant at the droplet's surface. This happens in droplets driven by Belousov-Zhabotinsky (BZ) reactions [19, 20]. We propose hereby a numerical treatment for a simplified scenario, where the chemical reactions change the nature of the surfactant itself. We consider two surface concentration fields instead of one, namely Γ_f , designating the "fresh" surfactants and Γ_w , designating a transformed state of the surfactant, the "waste". The surfactant in the bulk are in the fresh-state; they are adsorbed at the surface, then transformed into waste, which is, in return, desorbed into the bulk. While both fresh and waste-surfactants contribute to the surface saturation, only the fresh surfactants contribute to the surface tension. Hence in Langmuir equation (8), Γ is replaced by Γ_f . For each of the two fields we solve an equation of the kind of Eq. (24), with j_f and j_w (for the fresh and waste-surfactants respectively) instead of j

$$j_f = r_a[\Gamma_\infty - (\Gamma_f + \Gamma_w)]c_I - r_c\Gamma_f \quad (37)$$

$$j_w = -r_d\Gamma_w + r_c\Gamma_f \quad (38)$$

with r_c the constant chemical conversion rate. We neglect the advection-diffusion process of the waste-surfactant in the bulk and we take c as the bulk concentration of fresh surfactant. Hence, instead of Eq. (32), the Neumann boundary condition for c at the droplet's interface will read

$$D(\mathbf{n} \cdot \nabla c)|_I = j_f \quad (39)$$

The numerical treatment for all the concentration fields is the same as outlined in Sec. II C.

III. VALIDATION

We present here several test cases, separately addressing different aspects of the model. In the figures, the asterisks denote normalized quantities. The quantities used for the normalization, denoted by the subscript '0', are specified in the description of each test case.

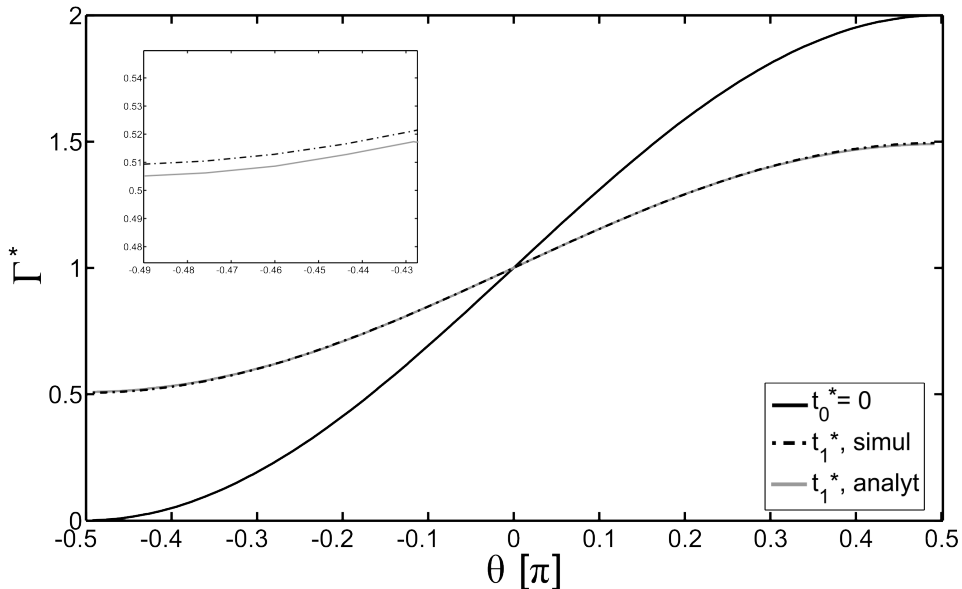


FIG. 4. Evolution of the surface concentration of a static undeformable droplet in the spherically-symmetric case, for the surface diffusion test described in Sec. III A. The black solid line depicts the initial distribution; after some time, namely at instant $t^* = 0.45$, the numerical results (black dash-dotted line) show a very good agreement with the analytical ones (grey solid line). Parameters: $R_0 = 6\mu\text{m}$, $\Gamma_0 = 3.4 \cdot 10^{-7} \text{kg/m}^2$, $D_s = 10^{-9} \text{m}^2/\text{s}$, $\epsilon = 1$, $\omega = 1$, $N_r = 100$, $N_z = 200$.

A. Surface diffusion

The present section tackles the surface diffusion of the surfactant (see Sec. II C 1). In particular, we test here the numerical solver (28) for the surface diffusion, described in Eq. (24). To this aim, we considered the case of a static, undeformable spherical droplet of radius R_0 , under the assumption of spherical-symmetry and no exchanges with the bulk ($j = 0$). We compared the numerical results with the analytical solution of the surface diffusion equation

$$\frac{\partial \Gamma}{\partial t} = D_s \nabla_s^2 \Gamma \quad (40)$$

with initial condition

$$\Gamma_0(\theta) = \Gamma_0 + \epsilon \sin(\omega\theta) \quad (41)$$

Here ϵ and ω are two constants and θ is the angular position, measured from the r axes in the counterclockwise direction (see Fig. 15). The analytical solution of Eq. (40) is

$$\Gamma(\theta, t) = \Gamma_0 + \epsilon \exp^{-2\omega^2 t/R_0^2} \sin(\omega\theta) \quad (42)$$

We found an excellent agreement between the numerical and the analytic results (see Fig. 4). In Fig. 5 we display the maximum absolute error of the surface concentration $\Gamma^* = \Gamma/\Gamma_0$ as a function of time, for different grid sizes: $N_r = 50$, $N_z = 100$ (solid line); $N_r = 100$, $N_z = 200$ (dash-dotted line), $N_r = 200$, $N_z = 400$ (solid line). As time progresses, a reduction of the grid size h of a factor 2 corresponds to circa a 4-times reduction in the error, as expected from a second-order method. The time and length scales used for the re-normalization in this test case are $t_\Gamma = R_0^2/D_s$ and R_0 respectively.

B. Surface advection and effect of the local change of curvature

In the present section we tested the advection of the surface concentration Γ and the effects of a local change of curvature at the interface on the field Γ (see Sec. II C 1, left hand side of Eq. (24)). To this aim, we considered the case of a deformable, spherical droplet with initial radius R_0 and uniform initial concentration Γ_0 . We prescribed a normal velocity field such that $\mathbf{u} = \mathbf{n}u_n$ and $u_n d = \text{const}$, with u_n the normal component of the velocity and $d = \sqrt{r^2 + z^2}$ the distance from the center of the

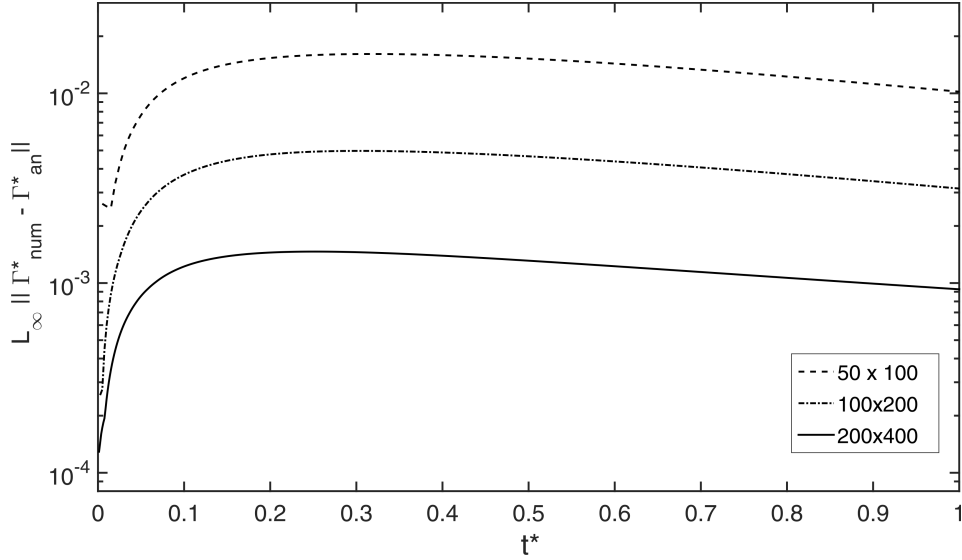


FIG. 5. Convergence test for surface diffusion: time evolution of the maximum absolute error $\|\Gamma_{num}^* - \Gamma_{an}^*\|$ on the surface concentration, for a static spherical droplet. Here the subscript *num* denotes the numerical results from simulations, *an* the analytical ones. Parameters: as in Fig. 4. The two lines represent different mesh resolutions: $N_r = 50, N_z = 100$ (dashed line); $N_r = 100, N_z = 200$ (dash-dotted line); $N_r = 200, N_z = 400$ (solid line). A reduction of the grid size h of a factor 2 produces a reduction of a factor around 4 in the error, as expected from a second-order method.

droplet. We neglected the surface diffusion as well as adsorption/desorption phenomena. With the latter assumption, the total mass of surfactant on the surface has to be conserved in time. Hence, the evolution of the field Γ is described by [55]

$$\frac{d(\Gamma A)}{dt} = 0 \quad (43)$$

where $A(t) = 4\pi R(t)^2$ is the area of the droplet and $R(t)$ is the radius at time t . Upon integration, one obtains

$$\Gamma(t) = \frac{A_0}{A(t)} \Gamma_0 \quad (44)$$

with A_0, Γ_0 the initial area and the initial concentration respectively. The analytical results were compared to the numerical ones, after deriving the average surface concentration at the droplet's surface Γ_{av} , at each time step as

$$\Gamma_{av} = \frac{\int_{S_{\text{drop}}} \Gamma dS}{S_{\text{drop}}} \quad (45)$$

with $S_{\text{drop}} = \int_{S_{\text{drop}}} dS$ the surface of the droplet. The integrals have been numerically calculated as [48]

$$\Gamma_{av} = \frac{\int_{\mathcal{D}} \delta_\epsilon(\Phi) \Gamma 2\pi r dr dz}{\int_{\mathcal{D}} \delta_\epsilon(\Phi) 2\pi r dr dz} \quad (46)$$

where \mathcal{D} is the computational domain and δ_ϵ is the smeared delta function Eq. (7). In Fig. 6 we display the time evolution of the average surface concentration, derived from simulations (black lines) for different grid sizes: 100x200 (dashed line) and 200x400 (dot-dashed line) computational cells. The numerical results are in excellent agreement with the analytical ones (light-grey solid line). In Fig. 7 the time evolution of the relative error on the average surface concentration is presented. When the grid size h is reduced of a factor 2, the error is reduced of a factor 5, compatibly with a second-order convergence of the method. The wavelength of the numerical oscillations in Fig. 7 is also reduced of a factor 2, as expected since the time step is

C. Bulk diffusion

In the present section we address the diffusion of the bulk concentration field c (see Sec. II C 2). In particular, we test the numerical solver (31) for the diffusion of the bulk concentration, described in Eq. (30), with Dirichlet boundary condition at the

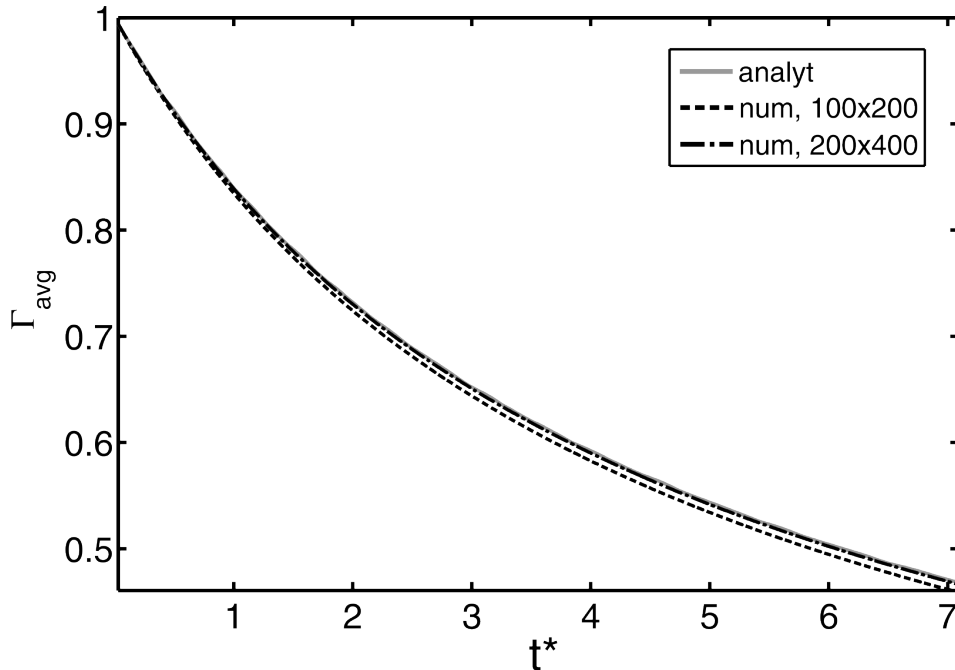


FIG. 6. Time evolution of the average surface concentration for a spherical expanding droplet. The numerical results (black lines) show a very good agreement with the analytical ones (grey solid line). Parameters: $R_0 = 1\mu\text{m}$, $\Gamma_0 = 1$. The different black lines represent different mesh resolutions: $N_r = 100, N_z = 200$ (dashed); $N_r = 200, N_z = 400$ (dash-dotted).

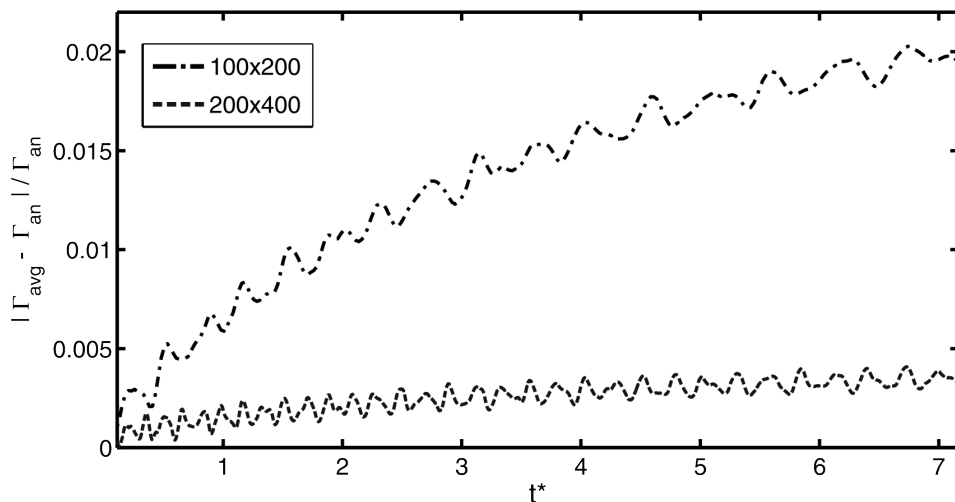


FIG. 7. Time evolution of the relative error between numerical and analytical results, for the average surface concentration of a spherical expanding droplet. Parameters: as in Fig. 6. The two lines represent different mesh resolutions: $N_r = 100, N_z = 200$ (dashed line); $N_r = 200, N_z = 400$ (dash-dotted line). A reduction of the grid size h of a factor 2 is associated to a reduction of a factor 5 in the error, compatibly with a second-order convergent method.

droplet's interface. To this aim we derived the analytical solution of the diffusion equation

$$\frac{\partial c}{\partial t} = D\nabla^2 c \quad (47)$$

on the outside of a spherical undeformable static sphere of radius R_0 in the spherically symmetric case. We took as boundary conditions $c = c_\infty$ in the far field (ideally $r \rightarrow \infty$) and Dirichlet boundary condition $c(t, R_0) = c_R$ at the droplet's interface. The initial condition was chosen as $c(t = 0) = c_\infty$ for $r > R$. The analytic solution of such a problem is

$$c_{an}(r, t) = \frac{R_0}{r} (c_R - c_\infty) \text{erfc}\left(\frac{r - R_0}{2\sqrt{Dt}}\right) + c_\infty \quad (48)$$

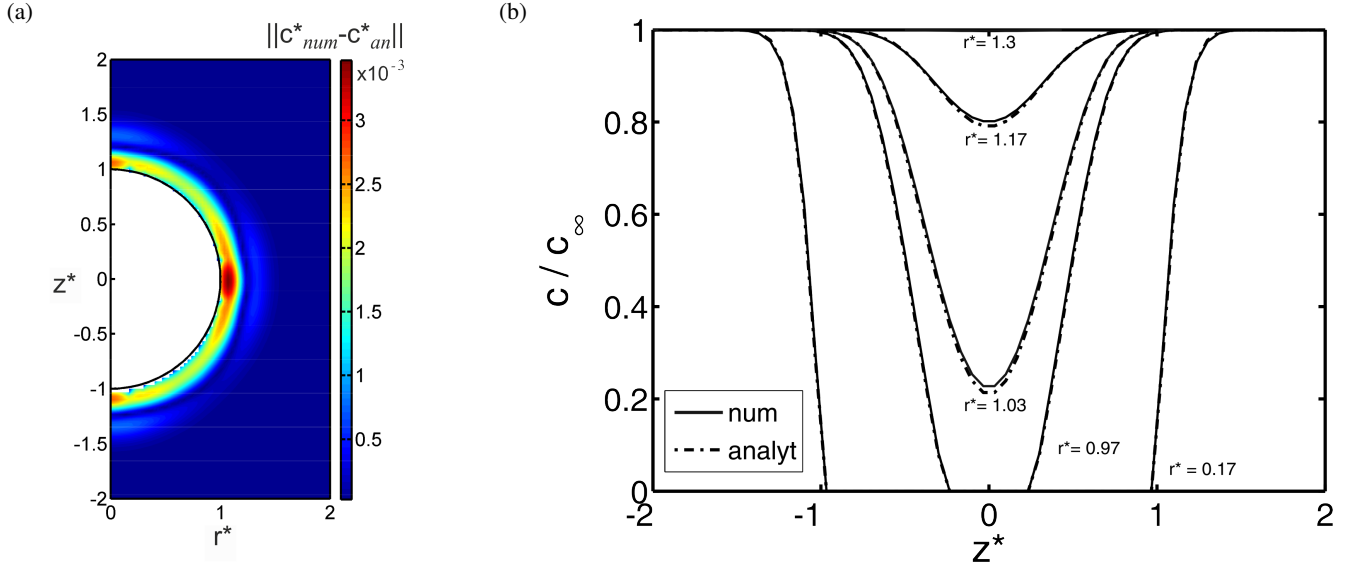


FIG. 8. Absolute error on $c^* = c/c_{\infty}$ between the analytical and the numerical solution for the diffusion equation in spherical coordinates, around a non-moving droplet of radius R , with initial condition $c(t=0, r) = c_{\infty}H(\Phi)$ and Dirichlet boundary condition $c(r=R_0) = c_R$ at the interface. Parameters: $R_0 = 25\mu\text{m}$, $c_{\infty} = 1$, $c_R = 0$, $N_r = 100$, $N_z = 200$ (a) absolute error at each point of the computational domain, at instant $t/t_D = 0.435$ (with $t_D = R_0^2/D$ the time scale for diffusion) (b) section of the numerical (solid lines) and analytical (dash-dotted lines) values of the bulk concentration, at time $t/t_D = 0.435$, along the z -axes for different values of $r^* = r/R$.

We found a very good agreement between analytical and numerical results (see Fig. 8). In Fig. 9 we show the maximum absolute value of the error between numerical and analytical results, respectively c_{num} and c_{an} , as a function of time, for different grid sizes. After an initial transient, reducing the grid size h of a factor 2 implies a reduction of a factor 4.5 in the error, as expected from a second-order method.

D. Adsorption-desorption

In the present section we test the solution of the bulk concentration diffusion equation, subject to Neuman boundary condition at the droplet's interface (see Sec. II C 2). We tackle the coupling between the surface concentration field Γ and the bulk concentration field c . In particular we address the adsorption-desorption mechanism described by Eqs. (25) and (32) and its numerical implementation Eq. (33).

1. Test 1. Residual method

We test hereby the numerical implementation (33) of the boundary condition (32), thus showing that the adopted numerical procedure is appropriate to address the Neumann boundary condition on the bulk concentration field c at the droplet's interface. To this aim, we adopted the following procedure. We neglected the advection of the liquid ($\mathbf{u} = 0$) and we considered the bulk diffusion equation, Eq. (47), in spherical coordinates in the case of a static, undeformable droplet of radius R_0 . In a general case, if a functional form for the concentration field is prescribed, $c^{\text{test}}(t, \mathbf{x})$, Eq. (30) will not be satisfied exactly, but a residual $f(t, \mathbf{x})$ will be present, such that

$$\frac{\partial c^{\text{test}}}{\partial t} = D\nabla^2 c^{\text{test}} + f(t, \mathbf{x}) \quad (49)$$

Similarly, the boundary condition at the droplet interface will be

$$\mathbf{n} \cdot \nabla c^{\text{test}}|_I = g(t, \mathbf{x}_I) \quad (50)$$

with $g(t, \mathbf{x}_I)$ a known function. If one solves numerically Eq. (49), with boundary condition Eq. (50) at the interface and initial condition $c^{\text{test}}(t=0, \mathbf{x})$, the prescribed c^{test} should be retrieved, instant by instant, a part from the error introduced by the

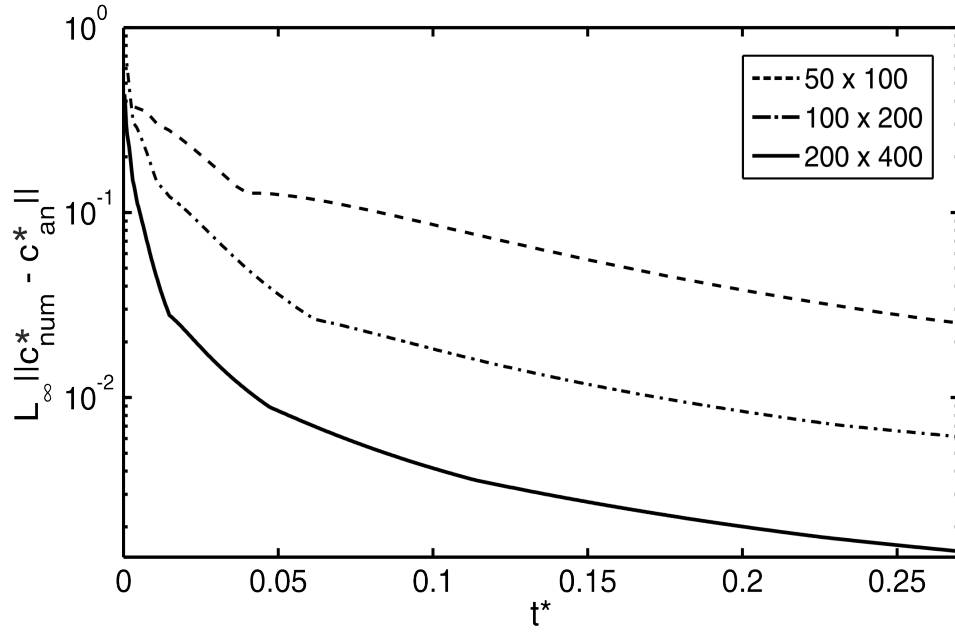


FIG. 9. Time evolution of the maximum absolute error between the numerical and the analytical solution, c_{num} and c_{an} respectively, of the bulk diffusion equation, around a static droplet of radius R_0 , with initial conditions $c(t=0) = c_\infty$ for $r > R_0$ and Dirichlet boundary condition $c(t, r = R_0) = c_R$ at the interface. Here $t^* = t/t_D$ is the normalized time, with $t_D = R_0^2/D$ the time scale for diffusion. Parameters: $R_0 = 25\mu\text{m}$, $c_\infty = 1$, $c_R = 0$. The different lines represent different mesh resolutions: $N_r = 50, N_z = 100$ (dashed); $N_r = 100, N_z = 200$ (dash-dotted); $N_r = 200, N_z = 400$ (solid). After an initial transient, a reduction of the grid size h of a factor 2 is associated to a reduction of a factor 4.5 in the error, as expected from a second-order method.

numerical method. Measuring this error and assessing its order of convergence will therefore indicate if the numerical method is really solving the equation that it is supposed to solve.

In our test case, we chose a function c^{test} satisfying the boundary conditions on the borders of the computational domain \mathcal{D} , i.e. such that $c^{test}|_{\partial\mathcal{D}} = 0$. In particular, we took the test function

$$c^{test}(t, \mathbf{x}) = \begin{cases} e^{-t} y e^{-\frac{1}{1-y}}, & \text{if } 0 < y < 1 \\ 0, & \text{else} \end{cases} \quad (51)$$

where $y = (r^2 + z^2 - R_0^2)/(L^2 - R_0^2)$, with R_0 the radius of the droplet and $L = 2R_0$. We substituted it inside Eq. (49) and Eq. (50), thus analytically deriving $f(t, \mathbf{x})$ and $g(t, \mathbf{x})$. By applying the numerical thick interface method described in II C to solve Eq. (49) with Neumann boundary condition Eq. (50), we then derived the numerical solution and we calculated the maximum absolute error respect to the exact one c^{test} . In Fig. 10 we show a comparison between numerical and analytical results of the concentration distribution along the first column of the computational domain (at $r = h/2$), for different time instants. The two provide good agreement. In Fig. 11 we plot the time evolution of such an error, for different grid sizes: $N_r = 100, N_z = 200$ (dash-dotted line), $N_r = 200, N_z = 400$ (solid line). After an initial transient, a reduction of the grid size h of a factor 2 implies a reduction of a factor 4 in the error, in agreement with a second order convergence of the method.

2. Test 2. Analytical solution (Muradoglu et al., J.Comput.Phys., 2008)

In the present test case, we address the solution of the bulk concentration diffusion equation, subject to a simplified Neumann boundary condition, where only adsorption occurs from the bulk to the surface and no desorption (Eq. (32), with $r_d = 0$). To this aim, we considered the case of a static undeformable spherical droplet of radius R , where only bulk diffusion and adsorption were present. Under these assumptions, the equation to be solved became

$$\frac{\partial c}{\partial t} = \frac{D}{r^2} \frac{\partial}{\partial r} \left(r^2 \frac{\partial c}{\partial r} \right) \quad (52)$$

with boundary condition at the interface $D\mathbf{n} \cdot \nabla c|_I = j$ and $j = r_a c_I$; therefore

$$\frac{d\Gamma}{dt} = r_a c_I \quad (53)$$

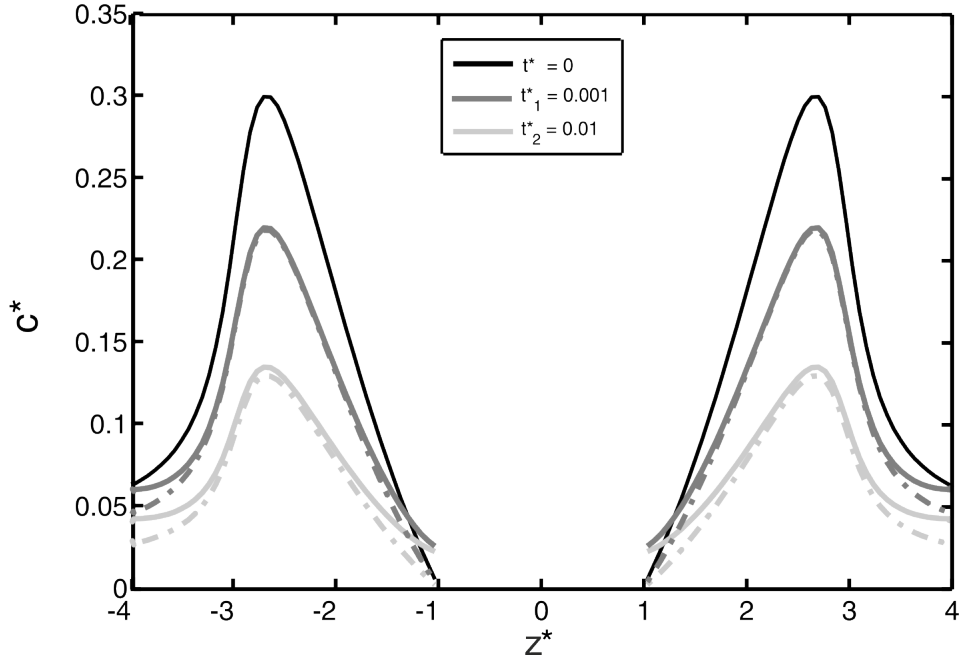


FIG. 10. Comparison of numerical (solid lines) and analytical (dash-dotted lines) results of residuals test for surfactants adsorption, as outlined in Sec. III D 1. The figure represents the bulk concentration distribution along the first column of the computational domain for different time instants: $t^* = 0$ (black), $t_1^* = 0.001$ (dark-grey) and $t_2^* = 0.01$ (light-grey). The axial coordinate is expressed as $z^* = z/R_0$. Parameters: $R = 6\mu\text{m}$, $N_r = 100$, $N_z = 200$.

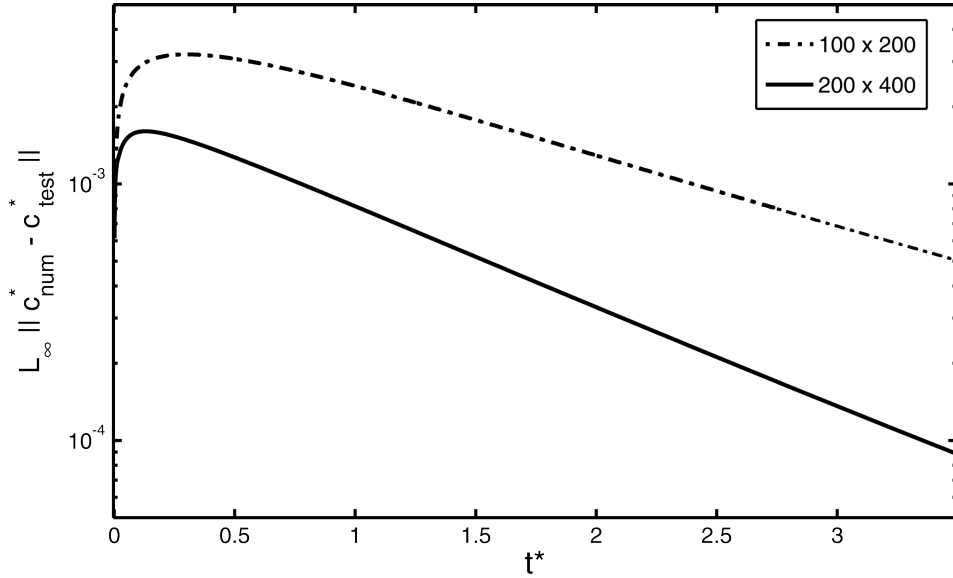


FIG. 11. Convergence test for residual test for surfactant adsorption, as outlined in Sec. III D 1: time evolution of the maximum absolute error on the bulk concentration, for a static undeformable spherical droplet of radius R_0 . Parameters: $R_0 = 6\mu\text{m}$. The different lines represent different mesh resolutions: $N_r = 100$, $N_z = 200$ (dash-dotted line), $N_r = 200$, $N_z = 400$ (solid line). A 2-times reduction of the grid size h corresponds to a 4-times reduction in the error, as expected from a second-order convergent method.

The bubble had an uniform initial surface concentration $\Gamma_0 = 0$. The initial bulk concentration was also uniform and equal to c_0 . An analytical solution of this set of equations has been derived for the case of an infinite domain in [55, 57]

$$\frac{c_0 - c}{c_0} = \frac{r_a \sqrt{\pi D t}}{D \left[1 + \frac{\sqrt{\pi D t}}{R} \left(1 + \frac{r_a R}{D} \right) \right]} \frac{R}{r} \operatorname{erfc} \left(\frac{r - R}{2\sqrt{D t}} \right) \quad (54)$$

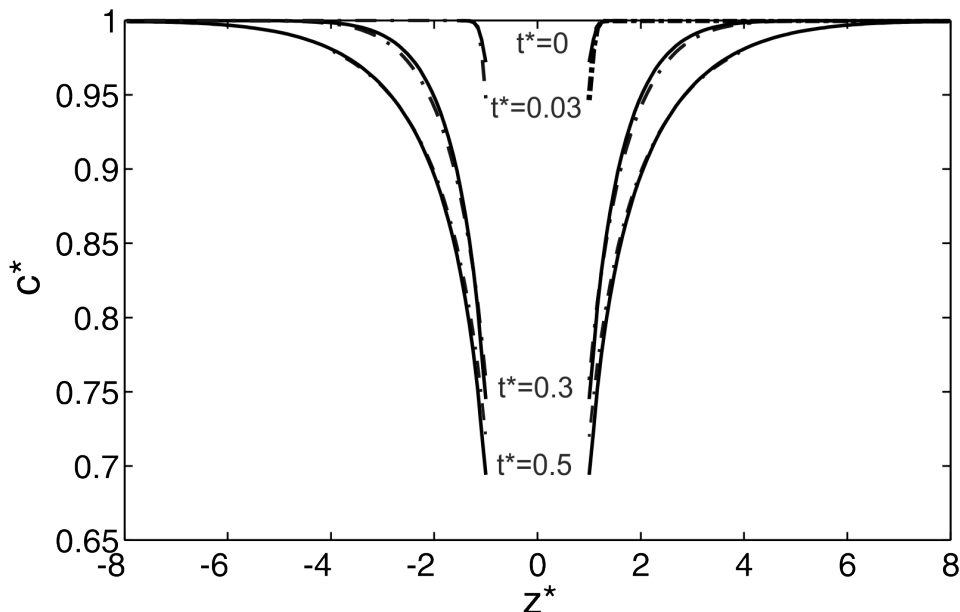


FIG. 12. Comparison of numerical and analytical results for the test for surfactant adsorption as outlined in Sec. III D 2. The figure represents the bulk concentration distribution along the first column of the computational domain for different time instants. The axial coordinate is expressed as $z^* = z/R_0$. Parameters: $R_0 = 6\mu\text{m}$, $N_r = 150$, $N_z = 300$.

It has been pointed out in [57], that such a solution is mostly valid for small times. The characteristic scales to use for the nondimensionalization of the equations in this test case are $L_0 = R_0$ for lengths and $T_0 = R_0^2/D$ for time. We found a good agreement between numerical and analytical results Fig. 12.

E. Marangoni test

In the present test, we address the flow solver described in Sec. II A as well as the numerical treatment of the kinematics II B of droplets moving by Marangoni flow, due to the presence of a non-uniform surface tension on the interface. To this aim, we consider a spherical undeformable droplet of radius R_0 , inside a cylindrical channel of length L . We impose a linear variation of the surface concentration field Γ , through the length of the channel, such that

$$\Gamma(z) = \Gamma_\infty \frac{z}{L} \quad (55)$$

where Γ_∞ is a constant. The surface tension obeys the law

$$\sigma(z) = \sigma_0 \left(1 - \beta \frac{\Gamma(z)}{\Gamma_\infty} \right) \quad (56)$$

in which σ_0 is the surface tension of a clean surface, μ is the viscosity of the fluid both outside and inside the droplet and β is a constant. The droplet is therefore expected to move along the concentration gradient, solely due to Marangoni stresses. For such a case, an analytical solution for the terminal velocity has been derived, under the approximation of Stokes flow [27, 55]

$$U_{an} = \frac{2\beta\sigma_0 R_0}{15L\mu} \quad (57)$$

In the simulation, we derived the value of the extrapolated field Γ at the center of each computational cell by first finding the closest point I of the interface, by means of Eq. (16) and using Eq. (55) with $z = z_I$. The velocity of the droplet at each time step was computed as

$$U = \frac{\int_{V_{\text{drop}}} u_z dV}{V_{\text{drop}}} \quad (58)$$

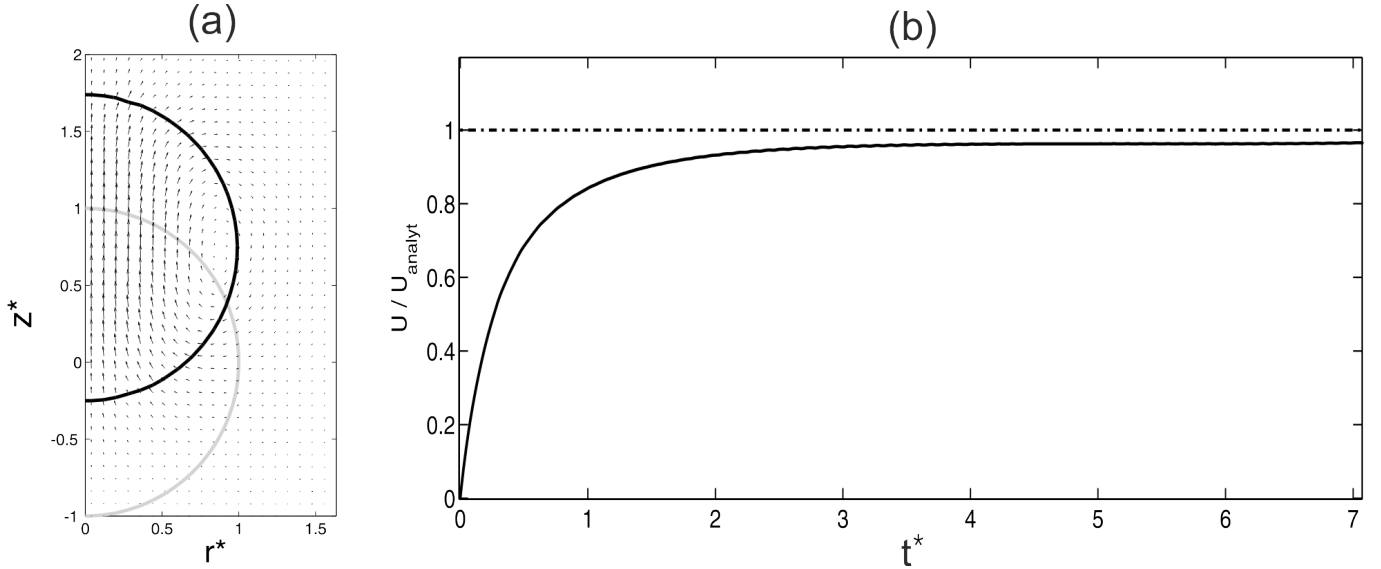


FIG. 13. Marangoni test for a spherical droplet immersed in a concentration gradient, as outlined in III E. Parameters: $R_0 = 6\mu\text{m}$, $\beta = 1$, $\sigma_0 = \Gamma_0 = 1$, $N_r = 100$, $N_z = 200$. (a) Velocity field at time $t_1^* = 6.04$ in the static frame of reference (arrows). The grey line represents the position of the droplet at time $t^* = 0$, the black line at $t^* = t_1^*$. (b) Time evolution of the average velocity from numerical simulations (solid line), in comparison to the analytical terminal velocity derived by Young et al. [27] (dash-dotted line). The difference lies within the 4%.

with u_z the vertical component of the velocity and $V_{\text{drop}} = \int_{V_{\text{drop}}} dV$ the volume of the droplet. The integrals have been numerically calculated as [48]

$$U = \frac{\int_{\mathcal{D}} [1 - H_\epsilon(\Phi)] u_z 2\pi r dr dz}{\int_{\mathcal{D}} [1 - H_\epsilon(\Phi)] 2\pi r dr dz} \quad (59)$$

where \mathcal{D} is the computational domain and H_ϵ is a smeared Heaviside function [61]

$$H_\epsilon(x) = \begin{cases} 0, & \text{if } x < -\epsilon \\ \frac{1}{2} \left(1 + \frac{x}{\epsilon} + \frac{1}{\pi} \sin \frac{\pi x}{\epsilon} \right), & \text{if } |x| \leq \epsilon \\ 1, & \text{if } x > \epsilon \end{cases} \quad (60)$$

The appropriate characteristic scales to use for the non-dimensionalization of the equations in this test case are $L_0 = R_0$ for the lengths and $T_0 = \sqrt{\frac{2\pi\rho R_0^2 L}{\beta\sigma_0}}$ for the time, corresponding to a displacement of around one radius length. In Fig. 13.a the grey line is the initial contour of the droplet, the black one is the contour at time $t_1^* = 6.04$. The black arrows represent the velocities at time t_1^* . In Fig. 13.b we show the time evolution of the average velocity of the droplet as derived from simulations (solid line), and we compare it with the analytical solution. With a computational grid of 100x200 cells, when the steady-state is reached, we find agreement within 3.5%.

F. Mass conservation

The level set method is known to suffer from artificial mass loss, mainly originating from the reinitialization step. In our treatment we address this problem, by using an extrapolated velocity field (built in the way described in Sec. II B) to advect the level set function, Eq. (15) and reducing the frequency of reinitialization steps. Thus we perform a reinitialization only when required (see Sec. II B). In this test, we wanted to assess the beneficial nature of this procedure. To this aim, we adopted the same setting of Sec. III E, a droplet moving due to Marangoni stresses, in response to a gradient in the surface concentration field. We examined the mass loss by tracking the change of volume, since the fluid density is constant in our setup. In Fig. 14 we display the time evolution of the relative error on the volume V , respect to the initial volume V_0 , for different numerical approaches: using the real velocity field \mathbf{u} to advect the interface and reinitializing at each time step (dash-dotted line); using the extended velocity field \mathbf{u}_{ext} , reinitialization every time step (dashed-line) or every 50 time steps (solid line). We show that, with the latter technique, it is possible to reduce the mass loss below 1% for a displacement of the droplet of around 10 radii, corresponding to several thousands of computational steps.

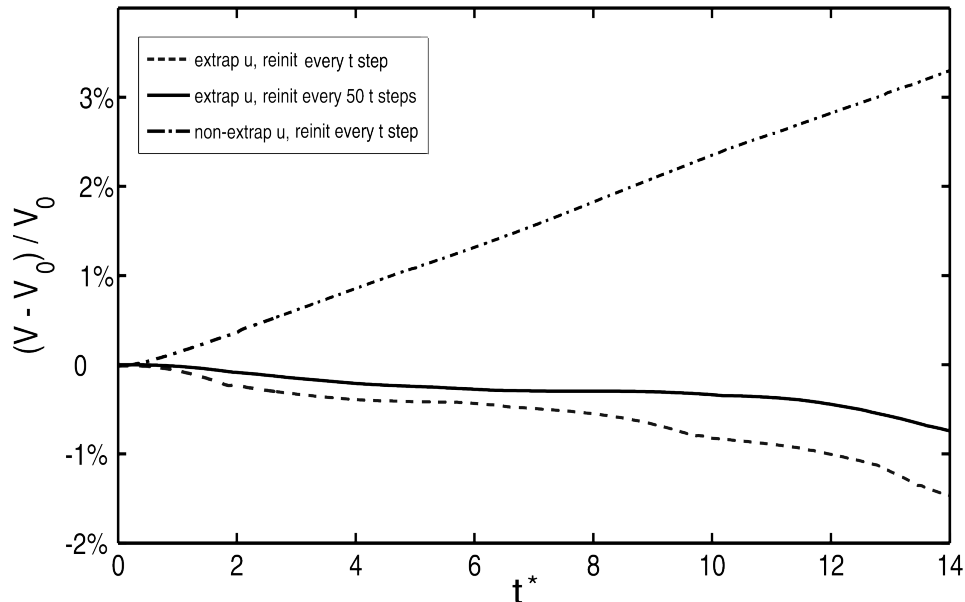


FIG. 14. Time evolution of the relative error on the droplet volume, representing the mass loss during the simulation of a droplet moving by Marangoni flow, described in Sec. III E. We show the results for different methods: using the real velocity field \mathbf{u} to advect the interface, reinitializing at each time step (dash-dotted line); using the extended velocity field \mathbf{u}_{ext} , reinitialization every time step (dashed-line) or every 50 time steps (solid line). In the last case the mass loss error is below 1% for a displacement of the droplet of around 10 radii.

IV. PROPULSION MECHANISMS

In the following section, we present several scenarios that may occur in the study of active droplets driven by Marangoni flow.

A. Pusher/puller behavior of "squirmers"

Several swimming microorganisms as well as artificial microswimmers can be described through the "squirmer" model [22], starting from a prescribed flow field at the interface. In the present simulation, we reproduce this standard behavior without directly prescribing a surface flow, but a surface tension distribution instead. In particular, we considered the case a spherical droplet of radius R_0 and we derived the velocity field originating from a non-uniform surface tension distribution. To this aim, we disregarded the surfactant fields both in the bulk and in the surface, and we prescribed a surface tension field $\sigma(\theta) = \sigma_0(1 + \epsilon \sin \theta/2)$, where θ was the angular position with respect to the radial axes, in the counterclockwise direction. The characteristic scales are $L_0 = R_0$ for the length and $t_0 = \sqrt{\pi R_0^3 \rho / 2 \epsilon \sigma_0}$ for the time, as t_0 gives an estimate of the time required to produce a displacement R_0 due to Marangoni flow. In Fig. 15, the black line (blue online) represents the initial position of the droplet, the light-grey line (green online) represents the contour of the droplet, almost undeformed, at time $t_1^* = 0.1$. The arrows depict the velocity field \mathbf{u} in the fixed frame of reference, i.e. in the lab frame, at time t_1^* . The exhibited behavior is typical of the so-called "neutral squirmers" [22], as the fluid is pushed away from the droplet at the leading edge (in the front), and is pulled towards the droplet at the trailing edge (in the back).

In Fig. 16 we show that, by prescribing a surface tension field $\sigma(\theta) = \sigma_0[1 + \epsilon \cos \theta \pm \sin(2\theta)]$, it is possible to reproduce the typical behavior of squirmers [22] acting as "pullers" (left figure, corresponding to the sign $+$) and "pushers" (right figure, corresponding to the sign $-$). At the droplet's trailing and leading edge the fluid velocity has indeed inward orientation respect to the interface, for the puller, outward for the pusher. The black lines (blue online) display again the initial position, the light-grey lines (green online) the position of the droplet at time $t_1^* = 0.1$. The arrows represent the velocity field in the co-moving frame of reference, displacing with the droplet. These velocities were calculated by subtracting the average velocity of the droplet, as derived by Eq. (59), from the velocity field \mathbf{u} .

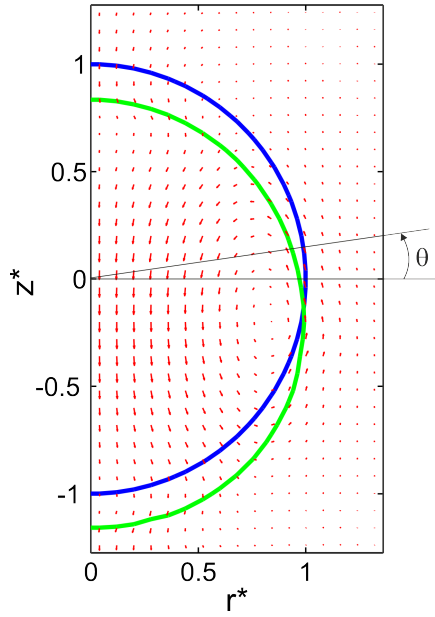


FIG. 15. Numerical simulation of a droplet moving downwards by Marangoni flow, when a surface tension field is prescribed as $\sigma(\theta) = \sigma_0(1 + \epsilon \sin \theta/2)$. Parameters: $R_0 = 25\mu\text{m}$, $\epsilon = 0.5$, $N_r = 50$, $N_z = 100$. The black line (blue online) represents the initial position, the light-grey line (green online) the position of the droplet at time $t_1^* = 0.1$. The arrows depict the velocity of the flow in the fixed reference frame.

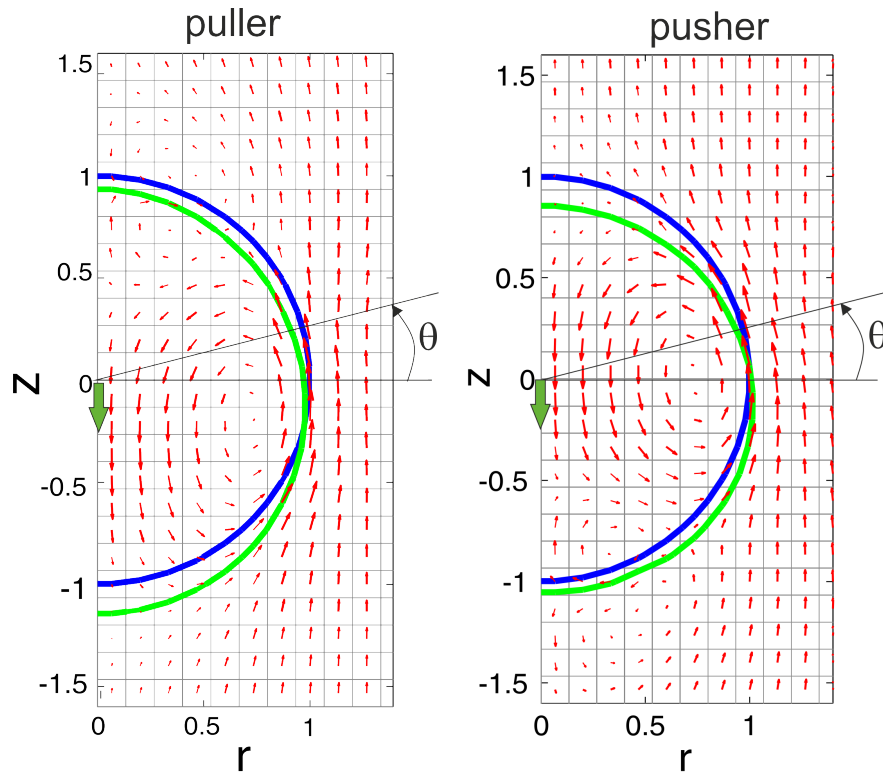


FIG. 16. Numerical simulation of a droplet moving by Marangoni flow in the downward direction, when a surface tension field is prescribed as $\sigma(\theta) = \sigma_0(1 + \epsilon \cos \theta \pm \sin(2\theta))$. The sign $+$ corresponds to the figure on the left, the $-$ to the figure on the right. Parameters: $R_0 = 25\mu\text{m}$, $\epsilon = 0.4$. The blue lines represent the initial position, the green lines the position of the droplet at time $t^* = t/t_0 = 0.12$. The thin arrows (red online) depict the velocity of the flow in the co-moving frame, shifting with the droplet. The two thick arrows (green online) indicate the direction of the droplet's motion. The two droplets reproduce the typical puller (left), pusher (right) behavior exhibited by squirmers.

B. Insoluble surfactants, advection and diffusion

In the following simulation, we consider the case of a droplet moving by Marangoni flow, with two non-interacting concentration fields, one covering the surface, Γ , the other, c , dissolved in the surrounding liquid. From the physical point of view, such a situation can occur when an insoluble surfactant covers the surface and a second specie is dissolved in the bulk, in equilibrium condition with the content of the droplet (e.g. liquid crystals in the emulsion droplets of [20]). This test case tackled the advection of the concentration fields, due to the motion of the droplet itself. Since the surfactants were taken as insoluble, no exchange with the bulk was present and $j = 0$ in Eq. (24). We therefore examined the evolution of the concentration fields, for a spherical droplet of initial radius R_0 moving by Marangoni flow. The motion was externally prescribed, by imposing a surface tension field $\sigma(\theta) = \sigma_0(1 + \epsilon \sin \theta/2)$, which gave origin to a velocity profile like in Fig. 15. Thus, for this test case, the retroaction of the surfactant concentration on the surface tension Eq. (8) was disregarded. The initial bulk concentration field was taken as $c = c_\infty H(\Phi)$, while the initial surface concentration was uniform and equal to Γ_0 . The characteristic scales of the problem were $L_0 = R_0$ for the length, $t_0 = \sqrt{\pi R_0^3 \rho / 2 \epsilon \sigma_0}$ for the time and Γ_0 for the surface concentration. The concentration fields moved due to both advection and diffusion. By changing the diffusion constants D and D_s , which give an indication of the speed of the diffusive process, and keeping all the other parameters the same, different behaviors of the concentration fields were expected. To assess the effect of D on the time evolution of the bulk concentration field c , we prescribed an initial stepwise uniform bulk concentration equal to c_∞ for $r > R_0$, c_R for $r = R_0$. We then examined the bulk concentration field after some time, for different values of D . In Fig. 17.a advection dominates over diffusion ($D = 10^{-8} m^2/s$). In this case the dissolved species is mostly advected by the velocity field (see Fig. 15), but it does not have the time to diffuse. Therefore a neat wake is formed behind the droplet. In Fig. 17.b, advection and diffusion are both relevant ($D = 8.5 \cdot 10^{-7} m^2/s$): the final distribution is asymmetric respect to the equatorial plane of the droplet but a consistent smoothing of the initial field appears. In Fig. 17.c bulk diffusion dominates over advection ($D = 10^{-4} m^2/s$): the initial distribution of the dissolved species is smoothed out but still symmetric respect to the equatorial plane of the droplet, regardless of the fluid velocity field.

To assess the effect of the surface diffusivity D_s on the time evolution of the surface concentration field Γ , we adopted the same procedure, by prescribing an initial sinusoidal surface concentration field $\Gamma = \Gamma_0(1 + \epsilon \sin \theta)$ with $\epsilon = 1/2$ and examining the effects as the time passed, for different values of D_s . In Fig. 18.a surface diffusion appears to be dominant over advection ($D_s = 10^{-3} m^2/s$): the initial surface concentration (black line, blue online) is uniformly leveled and evolves in a purely diffusive fashion (light-grey line, green online), regardless of the fluid's motion. In Fig. 18.b-c ($D_s = 10^{-5} m^2/s$ and $D_s = 10^{-7} m^2/s$ respectively), advection is also relevant and the evolution of the surface concentration differs from the purely diffusive one. In these cases, surfactants are piled up at $\theta = \pi/4$ and $\theta = -\pi/2$, following the motion of the fluid along the interface (see the direction of the vortices in Fig. 15, for a droplet moving in the downwards direction).

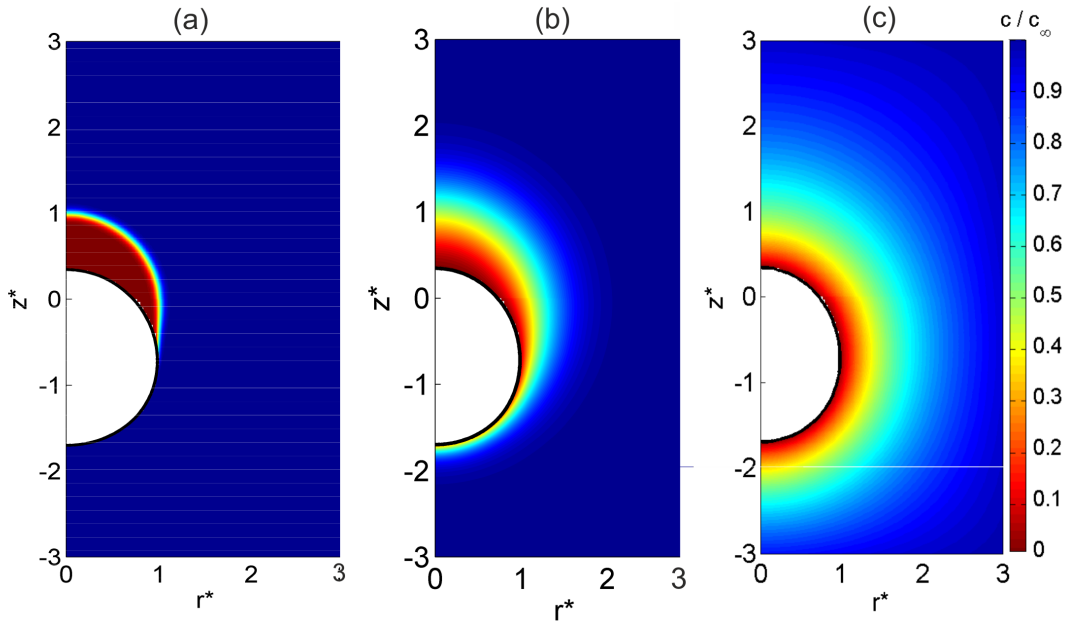


FIG. 17. Evolution of an initial bulk concentration field $c(t = 0, \mathbf{x}) = c_\infty H(\Phi)$ around a moving droplet, here depicted at time $t_1^* = 0.8$ for different values of the bulk diffusivity constant D . The motion of the droplet is prescribed and equal to the one described in Fig. 15. No coupling between the surface and the bulk is present (insoluble surfactants). (a) Low diffusive constant, advection dominates ($D = 10^{-8} \text{m}^2/\text{s}$) (b) Diffusion and advection are both relevant ($D = 8.5 \cdot 10^{-7} \text{m}^2/\text{s}$) (c) High diffusive constant, diffusion dominates ($D = 10^{-4} \text{m}^2/\text{s}$).

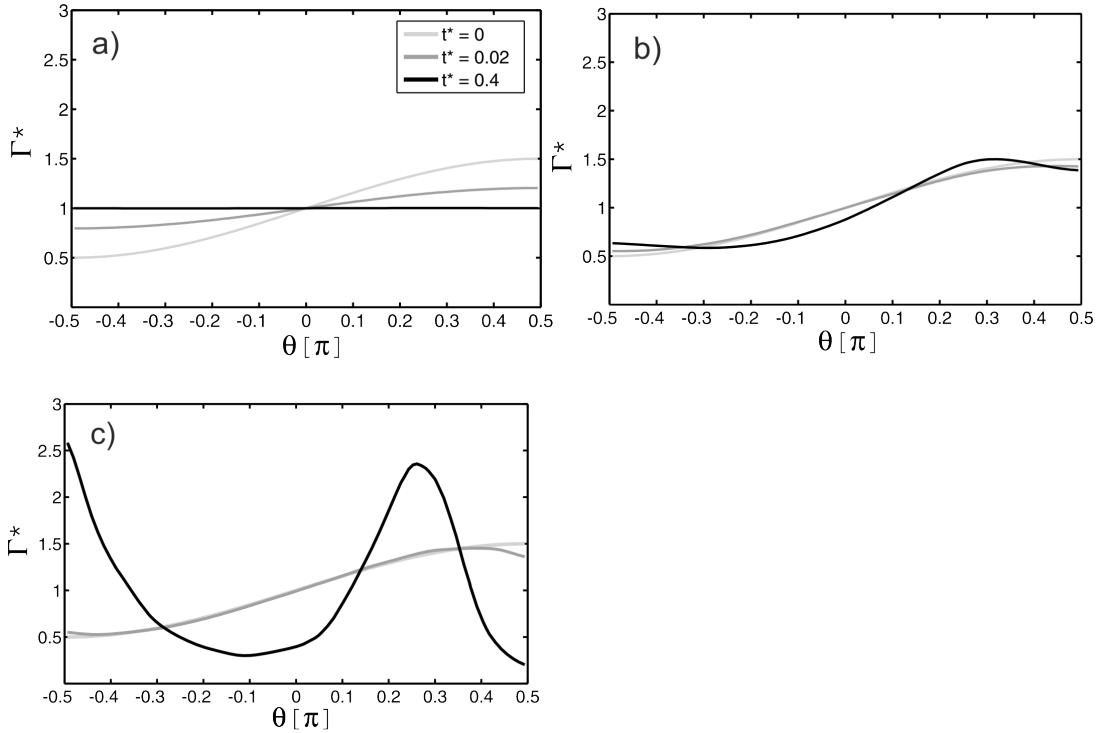


FIG. 18. Time evolution of an initial distribution of insoluble surfactants Γ (light-grey line) for different values of the surface diffusivity: (a) $D_s = 10^{-3} \text{m}^2/\text{s}$ (b) $D_s = 10^{-5} \text{m}^2/\text{s}$ (c) $D_s = 10^{-7} \text{m}^2/\text{s}$. The droplet is moving, due to a prescribed surface tension distribution, which induces a motion like the one depicted in Fig. 15. The different curves correspond to different time instants, as indicated in the legend.

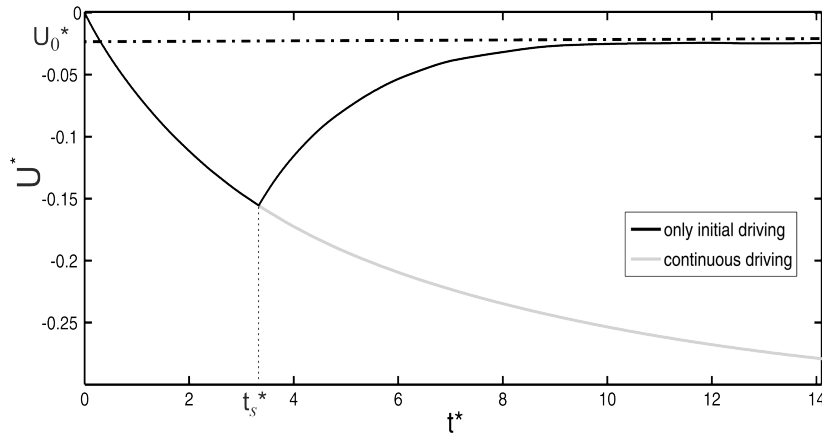


FIG. 19. Time evolution of the velocity of a droplet propelled by BZ-reactions. The motion is artificially initiated by prescribing a surface tension distribution like the one used in Fig. 15. The grey line represents a case where the external driving is preserved and the droplet keeps accelerating. The black line represents a case where the driving is turned off at time $t_s^* = 3.4$. The droplets decelerates, but it eventually reaches a steady-state velocity $U_0^* = -0.2$. Parameters: $D = 10^{-10} m^2/s$, $D_s = 10^{-9} m^2/s$, $R_0 = 6 \mu m$, $r_a = r_d = 1000$, $r_c = 10$.

C. BZ-reactions driven droplets

In these simulations, we considered a droplet with BZ reactions taking place on its surface, of the kind described in [20]. In particular, we wanted to assess the inception of a self-sustained propulsion mechanism, as a consequence of an initial perturbation (impulse), thus validating the simplified numerical treatment developed in Sec. II D. In order to mimic this scenario, we adopted the following procedure. The motion of the droplet was artificially initiated by prescribing a surface tension distribution $\sigma(\theta) = \sigma_0(1 + \epsilon \sin \theta/2)$, giving origin to a downwards oriented motion (see Fig. 15). The concentration fields were allowed to evolve according to their coupled advection-diffusion equations. However, for some time, the surface tension was still prescribed, thus acting as an external forcing, rather than being determined from the surface concentration of fresh surfactants. After some time, the artificial driving was switched off and, from that moment on, the surface tension distribution was derived by Langmuir equation (8). We observed that, after the removal of the forcing, the droplets kept moving, eventually reaching a non-null steady-state velocity. Hence, the initial perturbation initiated a self-sustained motion. In Fig. 19 we show the time evolution of the average velocity of the droplet, calculated by Eq. (57). The velocity is negative because the droplet is moving in the downward direction, along the z -axes. If the external forcing is not interrupted, the droplet keeps accelerating smoothly (grey line). If the external forcing is interrupted (black line) at time t_s^* , the droplet decelerates, but does not stop: the surfactants have self-organized in such a way that the motion continues, eventually reaching a steady-state velocity U_0^* .

In Fig. 20 we show the time evolution of the bulk concentration field, with realistic parameters for the diffusive constants $D = 10^{-10} m^2/s$ and $D_s = 10^{-9} m^2/s$. The droplet is moving in the downward direction. We notice that, in the wake of the droplet, there is an area where a lower surfactant concentration is present.

In Fig. 21.a the surface concentration fields of fresh surfactant Γ_f^* (solid lines), and waste surfactant Γ_w^* (dashed lines), are depicted, at different instants. Fig. 21.b displays the corresponding surface tension distributions. A gradient of fresh surfactant, thus of surface tension, originates as a consequence of the initial driving. As time passes, such a gradient persists, originating the self-propulsion mechanism of the droplet.

D. Chemotaxis

The purpose of the present simulations was to reproduce a typical chemotactic behavior, where a microswimmer moves along a gradient of chemical concentration and eventually slows down due to the inception of surface saturation. To this aim, we considered a spherical droplet of radius R_0 with adsorption/desorption of surfactant at the interface (soluble surfactants), but no chemical reactions. The droplet was introduced in a channel of length L , where a linear gradient of bulk concentration c was imposed

$$c(z) = c_\infty \frac{z}{L} \quad (61)$$

with c_∞ a constant. The droplet was expected to start moving in the upward direction, following the gradient, mimicking the behavior of several biological and artificial microswimmers. In Fig. 22 we display the time evolution of the average velocity of

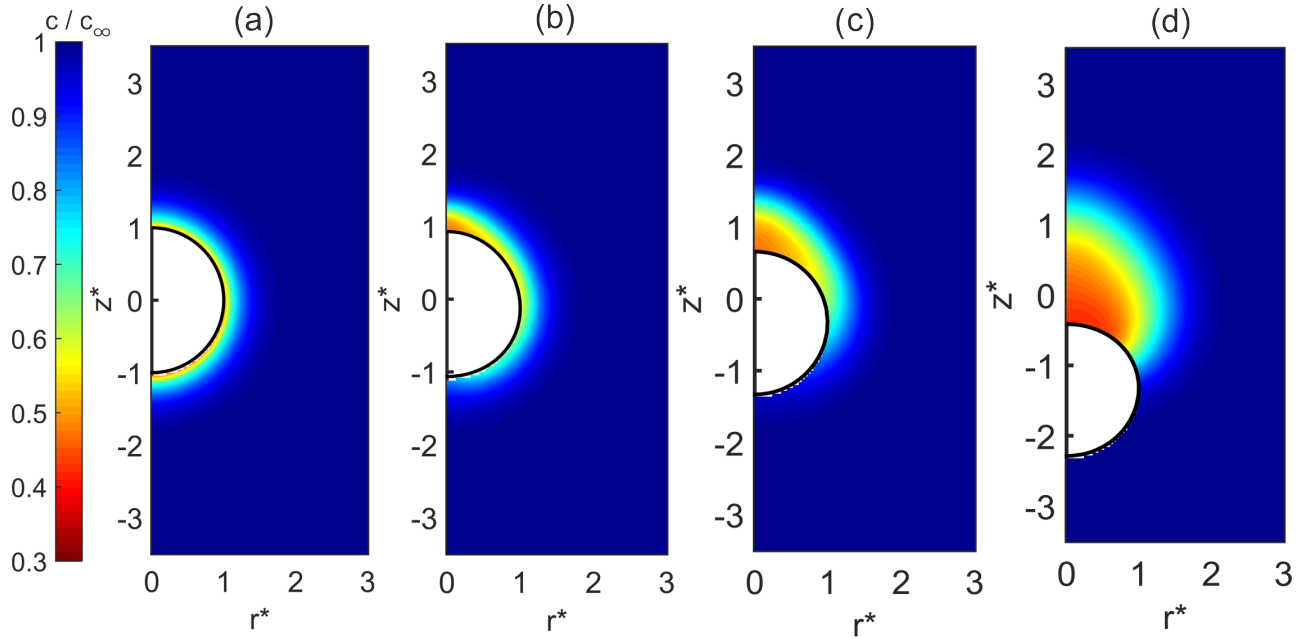


FIG. 20. Bulk concentration field of fresh surfactants c around the BZ-reactions driven droplet of Fig. 19, moving downwards, at different times (a) $t^* = 0$ (b) $t^* = t_s^* = 3.4$, when the external forcing is turned off (c) $t^* = 6.2$ (d) $t^* = 12.5$. Parameters: as in Fig. 19. A decumulation area of the surfactant appears in the wake of the droplet.

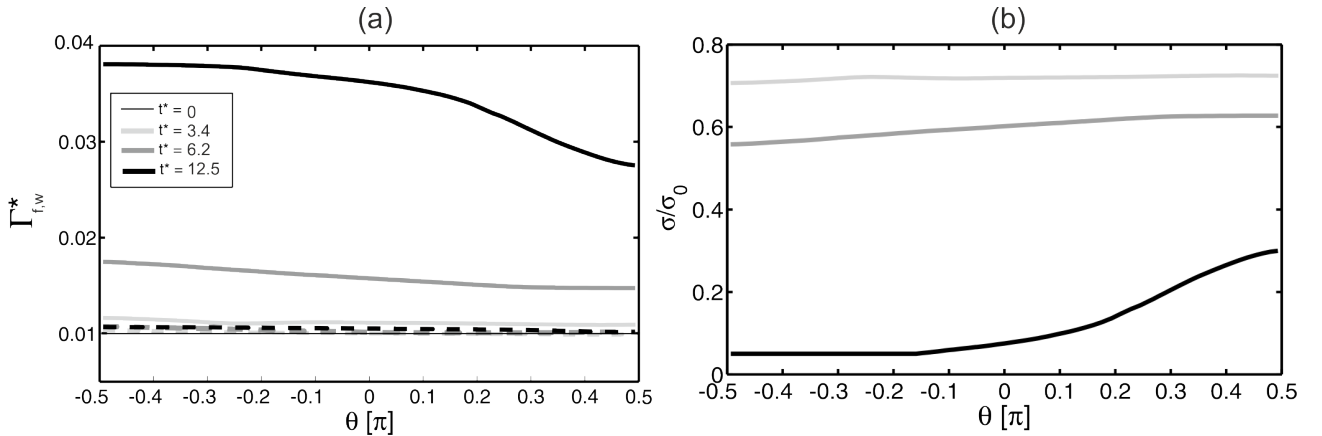


FIG. 21. (a) Surface concentration field of fresh surfactants Γ_f^* (solid lines) and waste surfactants Γ_w^* (dashed lines) and (b) surface tension for a BZ-reactions driven droplet. The different colours represent different times $t^* = 0$ (thin black lines) $t^* = 3.4$ (light-grey lines) $t^* = 6.2$ (dark-grey lines) $t^* = 12.5$ (black lines). Parameters: as in Fig. 19.

the droplet, as calculated by Eq. (57). The droplet immediately started moving in the expected direction (upwards, along the gradient), accelerating. The surfactant was adsorbed at the surface, thus reducing the surface tension until this reached, first only in some parts (at time t_σ^*), then everywhere, its minimum possible value ϵ_σ , according to Eq. (9). Therefore after time t_σ^* , the surface concentration started to decelerate due to the inception of saturation.

V. CONCLUSIONS

In this paper we considered the numerical study of artificial microswimmers, consisting of microdroplets moving by Marangoni flow, such as liquid crystal emulsion droplets [21] and BZ-reactions-driven droplets [20]. A detailed description of such systems lays beyond the scope of the present work, their complexity arising from the coexistence of an hydrodynamic motion, adsorption/desorption of surfactants at the interface, as well as reactions of different species, so that one has to deal with mutually interacting concentration fields. The aim of the present work was to provide a numerical treatment for the main

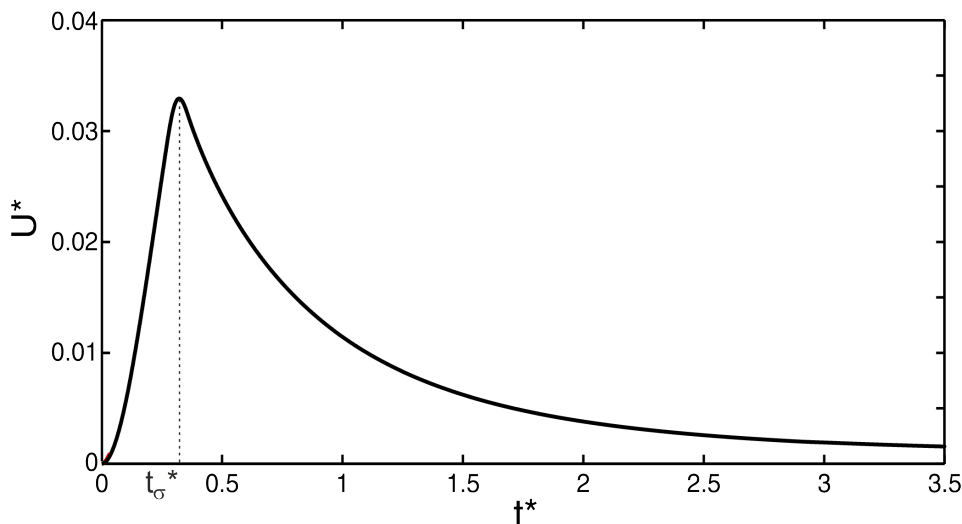


FIG. 22. Time evolution of the average velocity of a droplet with adsorption-desorption of surfactant, immersed in a linear gradient of surfactants in the bulk 61. The droplet starts to accelerate along the gradient, in the upward direction, but eventually slows down, starting from time t_{σ}^* , due to the inception of surface saturation. Parameters: $R_0 = 6\mu\text{m}$, $L = 60\mu\text{m}$, $\beta_s = 1$, $r_a = 100$, $r_d = 10$, $c_{\infty} = 10^{-6}\text{mol}/\text{m}^3$.

phenomena playing a role in the above-mentioned systems. We developed a second-order level-set model based on a continuous surface force approach. The main elements of the model are mass and momentum conservation, advection-diffusion of concentration fields both in the bulk (liquid surrounding the droplet) and on the droplet's surface. For the interaction between the bulk and the surface we considered several cases: a. the active exchange of surfactants between the bulk and the surface b. a concentration field dissolved in the liquid and in equilibrium with the content of the droplet (applicable to the behavior of liquid crystals based systems [20]). We also implemented a simple treatment of BZ reactions depleting surfactant at the surface. The numerical results were validated by comparison with analytical test cases, showing a second-order convergence respect to the grid size. With the present model, we reproduced the typical pusher/puller behavior of "squirmers". We presented a possible mechanism for self-propulsion in BZ-reaction driven droplets, by artificially initiating the motion by means of an impulse. After the external forcing stopped, the droplet continued to move reaching a non-zero steady-state speed. We also reproduced a typical chemotactic behavior, where a microswimmer moves along a gradient of chemical concentration and eventually slows down due to the inception of surface saturation.

VI. ACKNOWLEDGMENTS

The research leading to these results has received funding from the People Programme (Marie Curie Actions) of the European Union's Seventh Framework Programme FP7/2007-2013/ under REA grant agreement n° [628154]. The author would like to express her gratitude to Jürgen Vollmer, James Sethian, Robert Saye, Andrea Prosperetti and Stephan Herminghaus for insightful discussions and feedback on the manuscript. She would also like to acknowledge the hospitality at the Lawrence Berkeley National Laboratories (Berkeley, CA), where part of this research has been carried out.

-
- [1] E. M. Purcell, "Life at low Reynolds numbers," *Am. J. Phys.*, vol. 45, no. 1, pp. 3–11, 1977.
 - [2] H. Stark, "Immer in Bewegung bleiben: Die sonderbare Welt der kleinen Reynoldszahlen," *Physik J.*, vol. 6, no. 11, pp. 31–37, 2007.
 - [3] J. Gray, "Animal locomotion," 1969.
 - [4] J. Lighthill, *Mathematical Biofluidynamics*. Philadelphia: SIAM, 1975.
 - [5] E. Lauga and T. Powers, "The hydrodynamics of swimming microorganisms," *Rep. Prog. Phys.*, vol. 72, no. 9, p. 0966021, 2009.
 - [6] L. J. Fauci and R. Dillon, "Biofluidmechanics of reproduction," *Annu. Rev. Fluid Mech.*, vol. 38, pp. 371–391, 2006.
 - [7] D. Bray, *Cell movements*. New York: Garland Publishing, 2000.
 - [8] R. Dreyfus, J. Baudry, M. L. Roper, M. Fermigier, H. Stone, and J. Bibette, "Microscopic artificial swimmers," *Nature*, vol. 437, no. 7060, pp. 862–865, 2005.
 - [9] G. Ozin, I. Manners, S. Fournier-Bidoz, and A. Arsenault, "Dream nanomachines," *Adv. Mater.*, vol. 17, p. 3011, 2005.
 - [10] D. A. Saville, "The effects of interfacial tension gradients on the motion of drops and bubbles," *Chem. Eng. J.*, vol. 5, no. 3, pp. 251–259, 1973.

- [11] M. M. Hanczyc, T. Toyota, T. Ikegami, N. Packard, and T. Sugawara, "Fatty acid chemistry at the oil-water interface: Self-propelled oil droplets," *J. Am. Chem. Soc.*, vol. 129, pp. 9386–9391, 2007.
- [12] S. Thutupalli, R. Seemann, and S. Herminghaus, "Swarming behavior of simple model squirmers," *New J. Phys.*, vol. 13, p. 073021, 2011.
- [13] T. Banno, R. Kuroha, and T. Toyota, "pH-sensitive self-propelled motion of oil droplets in the presence of cationic surfactants containing hydrolyzable ester linkages," *Langmuir*, vol. 28, no. 2, pp. 1190–1195, 2012.
- [14] T. Ban, T. Yamagami, H. Nakata, and Y. Okano, "pH-dependent motion of self-propelled droplets due to Marangoni effect at neutral pH," *Langmuir*, vol. 29, no. 8, pp. 2554–2561, 2013.
- [15] T. Toyota, H. Tsuha, K. Yamada, K. Takakura, T. Ikegami, and T. Sugawara, "Listeria-like motion of oil droplets," *Chem. Lett.*, vol. 35, no. 7, pp. 708–709, 2006.
- [16] T. Toyota, N. Maru, M. M. Hanczyc, T. Ikegami, and T. Sugawara, "Self-propelled oil droplets consuming "fuel" surfactant," *J. Am. Chem. Soc.*, vol. 131, no. 14, pp. 5012–5013, 2009.
- [17] S. Thakur, P. B. S. Kumar, N. V. Madhusudana, and P. A. Pullarkat, "Self-propulsion of nematic drops: Novel phase separation dynamics in impurity-doped nematogens," *Phys. Rev. Lett.*, vol. 97, no. 11, p. 115701, 2006.
- [18] D. Molin, R. Mauri, and V. Tricoli, "Experimental evidence of the motion of a single out-of-equilibrium drop," *Langmuir*, vol. 23, no. 14, p. 7495, 2007.
- [19] H. Kitahata, N. Yoshinaga, K. H. Nagai, and Y. Sumino, "Spontaneous motion of a droplet coupled with a chemical wave," *Phys. Rev. E*, vol. 84, p. 015101, 2011.
- [20] S. Thutupalli and S. Herminghaus, "Oscillation patterns in active emulsion networks," 2012.
- [21] K. Peddireddy, P. Kumar, S. Thutupalli, S. Herminghaus, and C. Bahr, "Solubilization of thermotropic liquid crystal compounds in aqueous surfactant solutions," *Langmuir*, vol. 28, pp. 12426–12431, 2012.
- [22] Lighthill, "On the squirming motion of nearly spherical deformable bodies through liquids at very small Reynolds numbers," *Commun. Pure Appl. Math.*, vol. 5, no. 2, pp. 109–118, 1952.
- [23] J. R. Blake, "A spherical envelope approach to ciliary propulsion," *J. Fluid Mech.*, vol. 46, pp. 199–208, 1971.
- [24] T. Ishikawa, M. P. Simmonds, and T. J. Pedley, "Hydrodynamic interaction of two swimming model micro-organisms," *J. Fluid Mech.*, vol. 568, pp. 119–160, 2006.
- [25] I. Llopis and I. Pagonabarraga, "Hydrodynamic interactions in squirmer motion: Swimming with a neighbour and close to a wall," *J. Non-Newt. Fluid Mech.*, vol. 165, no. 17-18, pp. 946–952, 2010.
- [26] T. Ishikawa and T. J. Pedley, "Coherent structures in monolayers of swimming particles," *Phys. Rev. Lett.*, vol. 100, p. 088103, 2008.
- [27] N. O. Young, J. S. Goldstein, and M. Block, "The motion of bubbles in a vertical temperature gradient," *J. Fluid Mech.*, vol. 6, p. 350, 1959.
- [28] J. L. Anderson, "Colloid transport by interfacial forces," *Ann. Rev. Fluid. Mech.*, vol. 21, pp. 61–99, 1989.
- [29] S. Herminghaus, C. C. Maass, C. Krüger, S. Thutupalli, L. Goehringa, and C. Bahr, "Interfacial mechanisms in active emulsions," *Soft Matter*, vol. 10, pp. 7008–7022, 2014.
- [30] M. Schmitt and H. Stark, "Marangoni flow at droplet interfaces: Three-dimensional solution and applications," *Phys. Fluids*, vol. 28, p. 012106, 2016.
- [31] A. E. Rednikov, Y. S. Ryazantsev, and M. G. Velárde, "Drop motion with surfactant transfer in an inhomogeneous medium," *Int. J. Heat Mass Transf.*, vol. 37, pp. 361–374, 1994.
- [32] A. E. Rednikov, Y. S. Ryazantsev, and M. G. Velárde, "Drop motion with surfactant transfer in an homogeneous surrounding," *Phys. Fluids*, vol. 6, no. 2, pp. 451–468, 1994.
- [33] M. G. Velarde, A. Y. Rednikov, and Y. S. Ryazantsev, "Drop motions and interfacial instability," *J. Phys. Cond. Matt.*, vol. 8, no. 47, pp. 9233–9247, 1996.
- [34] N. Yoshinaga, K. H. Nagai, Y. Sumino, and H. Kitahata, "Drift instability in the motion of a fluid droplet with a chemically reactive surface driven by marangoni flow," *Phys. Rev. E*, vol. 86, no. 1, p. 016108, 2012.
- [35] M. Schmitt and H. Stark, "Swimming active droplet: A theoretical analysis," *Europhys. Lett.*, vol. 101, p. 44008, 2013.
- [36] G. Tryggvason, B. Bunner, A. Esmaeeli, D. Juric, N. Al-Rawahi, W. Tauber, J. Han, S. Nas, and Y.-J. Jan, "A front-tracking method for the computations of multiphase flow," *J. Comp. Phys.*, vol. 169, no. 2, pp. 708–759, 2001.
- [37] Y.-H. T. M.-C. Lai and H. Huang, "An immersed boundary method for interfacial flows with insoluble surfactant," *J. Comp. Phys.*, vol. 227, no. 15, pp. 7279 – 7293, 2008.
- [38] C. Pozrikidis, "A finite-element method for interfacial surfactant transport, with application to the flow- induced deformation of a viscous drop," *J. Eng. Math.*, vol. 49, no. 2, pp. 163–180, 2004.
- [39] A. J. James and J. Lowengrub, "A surfactant-conserving volume-of-fluid method for interfacial flows with insoluble surfactant," *J. Comp. Phys.*, vol. 201, no. 2, pp. 685–722, 2004.
- [40] S. Tasoglu and U. Demirci, "The effect of soluble surfactant on the transient motion of a buoyancy-driven bubble," *Phys. Fluids*, vol. 20, no. 4, p. 040805, 2008.
- [41] J. Xu, Z. Li, J. Lowengrub, and H. Zhao, "A level-set method for interfacial flows with surfactant," *J. Comput. Phys.*, vol. 212, pp. 590–616, 2006.
- [42] D. Adalsteinsson and J. A. Sethian, "Transport and diffusion of material quantities on propagating interfaces via level set methods," *J. Comp. Phys.*, vol. 181, no. 1, pp. 271–288, 2003.
- [43] X. Yang and A. J. James, "An arbitrary lagrangian-eulerian (ALE) method for interfacial flows with insoluble surfactants," *F. D. M. P.*, vol. 3, no. 1, pp. 65–95, 2007.
- [44] Y. P. C. Eggleton and K. Stebe, "Insoluble surfactants on a drop in an extensional flow: a generalization of the stagnated surface limit to deforming interfaces," *J. Fluid Mech.*, vol. 385, pp. 79–99, 1999.

- [45] S. Osher and J. A. Sethian, "Fronts propagating with curvature-dependent speed: Algorithms based on hamiltonjacobi formulations," *J. Comput. Phys.*, vol. 79, no. 1, pp. 12–49, 1988.
- [46] J. A. Sethian, *Level Set Methods and Fast Marching Methods Evolving Interfaces in Computational Geometry, Fluid Mechanics, Computer Vision, and Materials Science*. Cambridge University Press: Proc. Nat. Acad. Sci., 1999.
- [47] J. A. Sethian and P. Smereka, "Level set methods for fluid interfaces," *Annu. Rev. Fluid Mech.*, vol. 35, pp. 341–372, 2003.
- [48] S. Osher and R. Fedkiw, *Level set methods and dynamic implicit surfaces*. New York: Springer-Verlag, 2003.
- [49] J. Brackbill, D. Kothe, and C. Zemach, "A continuum method for modeling surface tension," *J. Comput. Phys.*, vol. 100, pp. 335–354, 1992.
- [50] A. J. Chorin, "Numerical solution of the Navier-Stokes equations," *Math. Comput.*, vol. 22, pp. 745–762, 1968.
- [51] J. A. Sethian and J. Strain, "Crystal growth and dendritic solidification," *J. Comp. Phys.*, vol. 98, pp. 231–253, 1992.
- [52] F. Gibou, L. Chen, D. Nguyen, and S. Banerjee, "A level set based sharp interface method for the multiphase incompressible Navier–Stokes equations with phase change," *J. Comp. Phys.*, vol. 222, pp. 536–555, 2007.
- [53] J.-D. Yu, S. Sakai, and J. A. Sethian, "Two–phase viscoelastic jetting," *J. Comp. Phys.*, vol. 220, pp. 568–585, 2007.
- [54] J. Zhang, D. Eckmann, and P. Ayyaswamy, "A front tracking method for a deformable intravascular bubble in a tube with soluble surfactant transport," *J. Comput. Phys.*, vol. 214, no. 1, pp. 366–396, 2006.
- [55] M. Muradoglu and G. Tryggvason, "A front-tracking method for computation of interfacial flows with soluble surfactants," *J. Comp. Phys.*, vol. 227, pp. 2238–2262, 2008.
- [56] U. Olgac and M. Muradoglu, "Computational modeling of unsteady surfactant-laden liquid plug propagation in neonatal airways," *Phys. Fluids*, vol. 25, p. 071901, 2013.
- [57] G. T. M. Muradoglu, "Simulations of soluble surfactants in 3d multiphase flow," *J. Comp. Phys.*, vol. 274, pp. 737–757, 2014.
- [58] K. E. Teigen, P. Song, and a. A. V. J. Lowengrub, "A diffuse-interface method for two-phase flows with soluble surfactants," *J. Comput. Phys.*, vol. 230, no. 2, pp. 375–393, 2011.
- [59] a. S. M. K.E. Teigen, "Influence of surfactant on drop deformation in an electric field," *Phys. Fluids*, vol. 22, p. 112104, 2010.
- [60] J. Xu and H. Zhao, "An Eulerian formulation for solving partial differential equations along a moving interface," *J. Sci. Comput.*, vol. 19, no. 1-3, pp. 573–594, 2003.
- [61] J. Xu, Y. Yang, and J. Lowengrub, "A level-set continuum method for two-phase flows with insoluble surfactant," *J. Comput. Phys.*, vol. 231, pp. 5897–5909, 2012.
- [62] Y. Pawar and K. Stebe, "Marangoni effects on drop deformation in an extensional flow: The role of surfactant physico-chemistry. I. Insoluble surfactants," *Phys. Fluids*, vol. 8, pp. 1738–1751, 1996.
- [63] E. Can and A. Prosperetti, "A level set method for vapor bubble dynamics," *J. Comp. Phys.*, vol. 231, no. 4, pp. 1533–1552, 2012.
- [64] D. Chopp, "Computing minimal surfaces via level set curvature flow," *J. Comput. Phys.*, no. 106, pp. 77–91, 1993.
- [65] M. Sussman, P. Smereka, and S. Osher, "A level set approach for computing solutions to incompressible two-phase flow," *J. Comput. Phys.*, no. 114, pp. 146–159, 1994.
- [66] J. A. Sethian, "A fast marching level set method for monotonically advancing fronts," *Proc. Nat. Acad. Sci.*, no. 93, pp. 1591–1595, 1996.
- [67] R. I. Saye, "High-order methods for computing distances to implicitly defined surfaces," *Comm. App. Math. and Comp. Sci.*, vol. 9, no. 1, pp. 107–141, 2014.
- [68] M. Sussman and E. Fatemi, "An efficient, interface-preserving level set redistancing algorithm and its applications to interfacial incompressible fluid flow," *SIAM J. Sci. Comput.*, vol. 20, pp. 1165–1191, 1999.
- [69] D. Adalsteinsson and J. A. Sethian, "The fast construction of extension velocities in level set methods," *J. Comp. Phys.*, vol. 148, no. 1, pp. 2–22, 1999.
- [70] H.-K. Zhao, T. Chan, B. Merriman, and S. Osher, "A variational level set approach to multiphase motion," *J. Comp. Phys.*, vol. 127, pp. 179–195, 1996.
- [71] D. Peng, B. Merriman, S. Osher, H. Zhao, and M. Kang, "A PDE-Based fast local level set method," *J. Comp. Phys.*, vol. 155, pp. 410–438, 1999.
- [72] D. Chopp, "Another look at velocity extension in the level set method," *SIAM J. Sci. Comput.*, vol. 31, no. 5, pp. 3255–3273, 2009.
- [73] G. S. Jiang and D. Peng, "Weighted ENO schemes for Hamilton Jacobi equations," *SIAM J. Sci. Comput.*, vol. 21, pp. 2126–2143, 2000.
- [74] G. R. and P. Smereka, "A remark on computing distance functions," *J. Comp. Phys.*, vol. 163, no. 1, pp. 51–67, 2000.
- [75] D. Enright, R. Fedkiw, J. Ferziger, and I. Mitchell, "A hybrid particle level set method for improved interface capturing," *J. Comput. Phys.*, vol. 183, pp. 83–116, 2002.
- [76] D. Chopp, "Some improvement of the fast marching method," *SIAM J. Sci. Comput.*, vol. 23, no. 1, pp. 230–244, 2001.
- [77] A. du Chene, C. Min, and F. Gibou, "Second order accurate computation of curvatures in a level set framework using novel high order reinitialization schemes," *SIAM J. Sci. Comput.*, vol. 35, pp. 114–131, 2007.
- [78] D. Adalsteinsson and J. A. Sethian, "A fast level set method for propagating interfaces," *J. Comp. Phys.*, vol. 118, pp. 269–277, 1995.
- [79] C. W. Shu and S. Osher, "Efficient implementation of essentially non oscillatory shock capturing schemes," *J. Comput. Phys.*, no. 77, pp. 439–471, 1988.
- [80] H. A. Stone, "A simple derivation of the time-dependent convective diffusion equation for surfactant transport along a deforming interface," *Phys. Fluids A*, vol. 2, no. 1, pp. 111–112, 1990.
- [81] T. Aslam, "A partial differential equation approach to multidimensional extrapolation," *J. Comput. Phys.*, vol. 193, no. 1, pp. 349–355, 2004.
- [82] D. M. E. J. Zhang and P. Ayyaswamy, "A front tracking method for a deformable intravascular bubble in a tube with soluble surfactant transport," *J. Comput. Phys.*, vol. 214, no. 1, pp. 366–396, 2006.